


May 2016

Impedance Spectroscopy Studies of Yttria Stabilized Zirconia Under Extreme Conditions

Quinlan Blaine Smith
University of Nevada, Las Vegas

Follow this and additional works at: <https://digitalscholarship.unlv.edu/thesesdissertations>

 Part of the [Condensed Matter Physics Commons](#), [Engineering Science and Materials Commons](#), and the [Materials Science and Engineering Commons](#)

Repository Citation

Smith, Quinlan Blaine, "Impedance Spectroscopy Studies of Yttria Stabilized Zirconia Under Extreme Conditions" (2016). *UNLV Theses, Dissertations, Professional Papers, and Capstones*. 2747.
<http://dx.doi.org/10.34917/9112194>

This Thesis is protected by copyright and/or related rights. It has been brought to you by Digital Scholarship@UNLV with permission from the rights-holder(s). You are free to use this Thesis in any way that is permitted by the copyright and related rights legislation that applies to your use. For other uses you need to obtain permission from the rights-holder(s) directly, unless additional rights are indicated by a Creative Commons license in the record and/or on the work itself.

This Thesis has been accepted for inclusion in UNLV Theses, Dissertations, Professional Papers, and Capstones by an authorized administrator of Digital Scholarship@UNLV. For more information, please contact digitalscholarship@unlv.edu.

IMPEDANCE SPECTROSCOPY STUDIES OF YTTRIA STABILIZED ZIRCONIA UNDER
EXTREME CONDITIONS

By

Quinlan B. Smith

Bachelor of Science - Physics
California Lutheran University
2012

A thesis submitted in partial fulfillment
Of the requirements for the

Master of Science – Physics

Department of Physics and Astronomy
College of Sciences
The Graduate College

University of Nevada, Las Vegas
May 2016

Copyright 2016 by Quinlan Smith

All Rights Reserved



Thesis Approval

The Graduate College
The University of Nevada, Las Vegas

April 11, 2016

This thesis prepared by

Quinlan B. Smith

entitled

Impedance Spectroscopy Studies of Yttria Stabilized Zirconia Under Extreme Conditions

is approved in partial fulfillment of the requirements for the degree of

Master of Science – Physics
Department of Physics and Astronomy

Michael Pravica, Ph.D.
Examination Committee Chair

Kathryn Hausbeck Korgan, Ph.D.
Graduate College Interim Dean

Andrew Cornelius, Ph.D.
Examination Committee Member

Stephen Lepp, Ph.D.
Examination Committee Member

Paul Forster, Ph.D.
Graduate College Faculty Representative

ABSTRACT

IMPEDANCE SPECTROSCOPY STUDIES OF YTTRIA STABILIZED ZIRCONIA UNDER EXTREME CONDITIONS

By

Quinlan B. Smith

Dr. Michael Pravica, Thesis Defense Committee Chair
University of Nevada, Las Vegas

Yttria Stabilized Zirconia (YSZ) is of interest for many industries. Varying amounts of Yttria (Y_2O_3) can be doped into Zirconia (ZrO_2) to create materials with specific characteristics. For instance, 3mol% YSZ (3YSZ) is known to be a super hard material and is used as a coating on drill tips and as an abrasive. Eight mol% YSZ (8YSZ) is commonly used as a solid electrolyte in Solid Oxide Fuel Cells because of its good ionic conducting abilities and stability at high temperatures. In this thesis project, a novel experimental setup was created and used to study the ionic conductivity of (3 and 8mol%)YSZ with pressure and temperature via *in situ* impedance spectroscopy measurements inside a diamond anvil cell. Pressures of 0-17GPa and temperatures in the range between 294-523k were achieved during the experiment. Additionally, a powder x-ray diffraction non-hydrostatic high-pressure structural study of the two samples was completed at High Pressure Collaborative Access Team (HP-CAT) Sector 16 at the Advanced Photon Source. It was observed that the ionic conductivity of both sample material decreased with increased pressure. The compression stress caused a decrease in cell volume and the distance between oxygen vacancy sites and mobile oxygen ions became closer. This reduction caused ionic conductivity to decrease.

ACKNOWLEDGEMENTS

I would like to thank Dr. Michael Pravica for advising me and giving me the ability and freedom to pursue novel independent research. I would like to thank Dr. John Howard for allowing me to use his laboratory equipment and collaborating with me. Also, I would like to thank my Masters committee for advising me through my research project. Additionally, I would like to thank the UNLV Department of Physics faculty and administrative assistants for educating and assisting me. I would like to thank the beam line scientists at HP-CAT for their support during this experiment. Lastly, I would like to thank my parents, Kay and Blaine Smith, for their encouragement and support. I would not be where I am today without them

TABLE OF CONTENTS

ABSTRACT.....	iii
ACKNOWLEDGEMENT	iv
LIST OF TABLES	vi
LIST OF FIGURES	vii
CHAPTER 1: INTRODUCTION	1
CHAPTER 2: BACKGROUND.....	4
CHAPTER 3: THEORY	8
IMPEDANCE SPECTROSCOPY	8
RUBY FLUORESCENCE	20
X-RAY POWDER DIFFRACTION	22
CHAPTER 4: EXPERIMENTAL.....	25
SAMPLE MATERIAL CHARACTERIZATION.....	25
HIGH-PRESSURE IMPEDANCE SPECTROSCOPY	25
NON-HYDROSTATIC HIGH PRESSURE POWDER XRD STUDY	30
CHAPTER 5: RESULTS AND DISCUSSION.....	31
HIGH-PRESSURE IMPEDANCE SPECTROSCOPY	31
NON-HYDROSTATIC HIGH PRESSURE POWDER XRD STUDY	40
CHAPTER 6: CONCLUSION	45
REFERENCES	46
CV	50

LIST OF TABLES

TABLE 2.1 YSZ Lattice Parameters	5
TABLE 3.1 Immitance Function Relations	9
TABLE 3.2 Bravais Lattices.....	24
TABLE 5.1 Fitted Resistance and Calculated Conductivities.....	36
TABLE 5.2 Pressure and Calculated Cell Volumes.....	43

LIST OF FIGURES

Figure 2.1 YSZ Cubic Structure	5
Figure 2.2 YSZ Phase Diagram	6
Figure 3.1 EIS Measurement Schematic.....	11
Figure 3.2 Resistor and Capacitor Impedance Spectra	13
Figure 3.3 Resistor and Capacitor in Series Impedance Spectra	14
Figure 3.4 Capacitor and Resistor in Parallel Impedance Spectra.....	15
Figure 3.5 Impedance Spectra of Homogenous Material	16
Figure 3.6 Modified Bauerle Proposed Circuit Impedance Spectra	17
Figure 3.7 Brick Layer Model	18
Figure 3.8 Energy Diagram of Ruby Fluorescence	20
Figure 3.9 Ruby Spectra	21
Figure 4.1 Merrell-Bassett Type Diamond Anvil Cell	26
Figure 4.2 Non-Conductive Gasket Schematic.....	27
Figure 4.3 Picture of Non-Conductive Gasket.....	28
Figure 4.4 EIS High-Pressure Experimental Set Up.....	29
Figure 4.5 Mao-Bell Type Diamond Anvil Cell.....	30
Figure 5.1 3YSZ Experimental Impedance Spectra	32
Figure 5.2 8YSZ Experimental Impedance Spectra	33
Figure 5.3 Equivalent Circuit and Fitting Equations	35
Figure 5.4 3YSZ EIS Sample Pictures.....	38
Figure 5.5 8YSZ EIS Sample Pictures.....	39
Figure 5.6 Arrhenius Plot of YSZ Conductivities	40

Figure 5.7 3YSZ and 8YSZ XRD Patterns	42
Figure 5.8 8YSZ Powder XRD Sample Picture.....	43
Figure 5.9 YSZ Equation of State.....	44

CHAPTER 1

INTRODUCTION

Yttria stabilized zirconia (YSZ) has become a material of major interest because of its structural, thermal, and ionic conducting properties. Due to its hardness, chemical inertness, and low cost, it is used as a tooth and bone replacements, as well as, a refractory for jet engines, and is the main material in ceramic knives and super hard drill tips [1]. Additionally, because of its stability and high ionic conductivity at high temperatures, YSZ can be used as a solid-state electrolyte for solid oxide fuel cells (SOFC's) operating in a temperature range of 1200-1500°C [2]. Furthermore the material can be used as a thermal barrier coating for jet engine blades [3]. The applications of YSZ in extreme environments is wide and varying, but to the best of the author's knowledge, there has not been an experiment that has investigated the behavior of this extremely important material under extreme pressures and temperatures. This thesis reports the first investigation of the ionic conductivity of polycrystalline 3, 8mol% of YSZ under pressures of 0-17GPa and temperatures of 25-250°C. The work most similar to this thesis is a paper that was published in 2002 that investigated the relationship between ionic conductivity and direction of stress on 3YSZ up to 800MPa and at temperatures up to 250°C [4]. Their experiment did not occur in a diamond anvil cell, but they concluded that resistance increases with the small pressures they applied. The goals of this thesis were to further investigate how the ionic conductivity can change with pressure and to obtain structure information of 3YSZ and 8YSZ at extreme pressures.

To obtain high pressures, both 3 and 8mol% YSZ were confined in a diamond anvil cell and, via resistive heating, heated to the desired temperatures. Electrical measurements and determination of total electrical conductivity of a system can be affected by sample geometry,

interfacial effects, intercrystalline barriers, space charge formation, relaxation, etc. Implementing the use of impedance spectroscopy over a wide range of frequencies can alleviate some of these issues [5,6]. Similarly, high-pressure environments can cause complex structural and electronic transformations that have large thermal and baric hysteresis, creating nano-crystalline structures [7]. Impedance spectroscopy is a powerful tool in its ability for investigating high-pressure phase transformations, phase stability, nucleation of new phases etc. [8] In this experiment, *in situ* impedance spectroscopy measurements were taken inside the diamond anvil cell with a Solatron® 1260 Impedance Gain/Phase Analyzer, to determine the ionic resistance of the sample materials under the non-hydrostatic pressure and temperature conditions. Additionally, a non-hydrostatic high-pressure structural study of 3 and 8mol% YSZ was completed at the BM-D beam line at HP-CAT Sector 16 of the Advanced Photon Source at Argonne National Laboratory.

Due to the complexity of high-pressure impedance spectroscopy experiments, there is not a plethora of past experiments to reference. One of the earliest papers researching this topic, *Vereshchagin et al* 1972, used polycrystalline diamonds with conductive paste between the grains, known as carbonado diamonds, as the electrical probes during their pressure [9]. Multiple other researchers have employed the same setup [11-14]. Additionally, other techniques have been implemented, like designer diamonds with the leads grown into the diamonds [15], sputter coating diamonds with Au/Ti [16], and silver [17]. Alumina sputter coating has also been employed to insulate the electrodes from the gasket and other conducting components of the diamond anvil cell. In this thesis, a modified version of the high-pressure DC electrical 4-probe conductivity technique was used similar to [18]. A nonconductive gasket was made out of c-BN, and platinum probes were placed on top and bottom of sample material. Ruby was used as a

pressure marker for this non-hydrostatic experiment. An impedance spectrum was measured over a frequency range of 20MHz-1Hz. In the experimental section, more details will be given on the exact experimental setup. In the results and discussion chapter, it will be shown that the ionic conductivity of both samples decreased with added pressure and no phase transitions were observed between the pressures of 0-26GPa.

CHAPTER 2

BACKGROUND

In this section, Yttria stabilized zirconia's structure, composition, conductivity, and applications will be discussed; as well as, any literature concerning YSZ that is related to this experiment and YSZ.

Yttria Stabilized Zirconia

Yttria stabilized zirconia consists of varying amounts of Yttria, Y_2O_3 , doped into Zirconia, ZrO_2 . 3mol% YSZ is well known for its strength and hardness [19], where as, 8%mol YSZ is known to be the best ionic conductor and the conductivity decreases with higher percentages of dopant [31]. Breaking down the compound into its components, pure zirconia, which is known as the mineral Baddeleyite, possesses three phase transitions with increase in temperature before melting. The three phases and their transition temperatures are monoclinic, $P2_1/c$, (ambient) \rightarrow tetragonal, $P4_2/nmc$ ($1170^\circ C$) \rightarrow cubic, $Fm3m$ ($2370^\circ C$) \rightarrow liquid ($2710^\circ C$) [20]. As more yttria (which is stable up to $1800^\circ C$ in air, is doped into the zirconia) tetragonal phases and cubic phases of the compound can be stable at ambient temperatures and pressures. The minimum doping to form the tetragonal YSZ, also known as partially stabilized zirconia (PSZ) is 2mol% yttria and to form the fully stabilized zirconia (FSZ) cubic structure is 8mol% yttria [21]. Figure 2.1 show yttria doped into zirconia to form cubic YSZ.

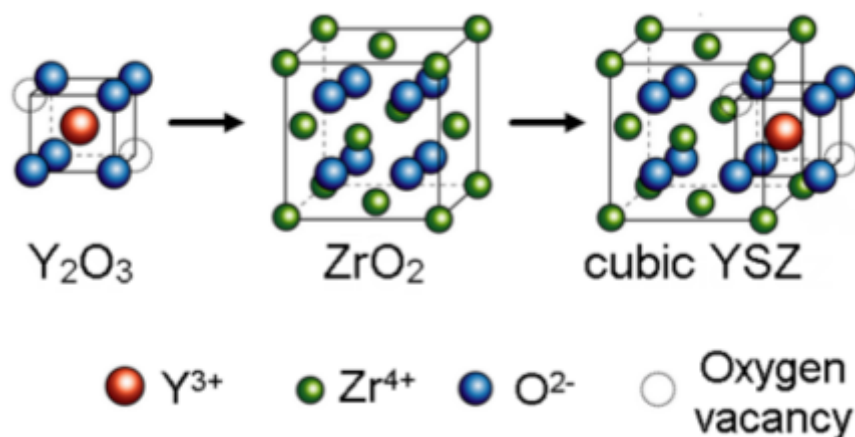


Figure 2.1: If 12% or more of yttria is doped into zirconia, cubic YSZ is formed.

There is much controversy on the exact amount of doping that can cause the stable tetragonal and cubic structures to form. Many papers claim that the YSZ does not become fully tetragonal until 3mol% and that a stable cubic structure is not achieved until 12mol% [23,24,25]. According to a recent publication, “X-ray diffraction study of compositionally homogenous, nano-crystalline yttria-doped zirconia powders” is the stable tetragonal phase, $P4_2/nmc$, exists at room temperature in YSZ when yttria doped in the 2.8-12mol% range [26].

Table 2.1 Lattice Parameters for Ambient YSZ

	m	t	t'	t''	c
Space group	$P2_1/c$	$P4_2/nmc$	$P4_2/nmc$	$P4_2/nmc$	$Fm3m$
a Å	5.156	3.64	3.5984	5.094	5.07
b Å	5.191				
c Å	5.304	5.27	5.1520	5.177	
c/a		1.448	1.432	1.016	1
β	98.9°	90°	90°	90°	90°
Coordination	7	8	8	8	8
ZrO ₂	4	2	2	4	4
Reference	34	35	36	37	38

According to Yashima *et al*, there are three tetragonal phases formed when doping Y_2O_3 into ZrO_2 , which are t, t' and t''-ZrO₂. All of these phases belong to the $P4_2/nmc$ space group as shown in Table 2.1 [34-38]. The idea is that doping of cations in low amounts can stabilize the tetragonal phases of t-ZrO₂ at room temperature. The YSZ t'-form ($c/a > 1$), where c/a is the axial

ratio between the tetragonal unit cell and the pseudo-fluorite cell that has been used in past literature, does not transform into the monoclinic ZrO_2 phase and remains metastable at high temperatures [27]. The t'' - ZrO_2 is metastable. However, it is also not as stable as the t' and the fluorite cubic phase. [28][29]. Although the exact doping percentages to create certain phases are still in contention, Figure 2.2 displays the most recent phase diagram.

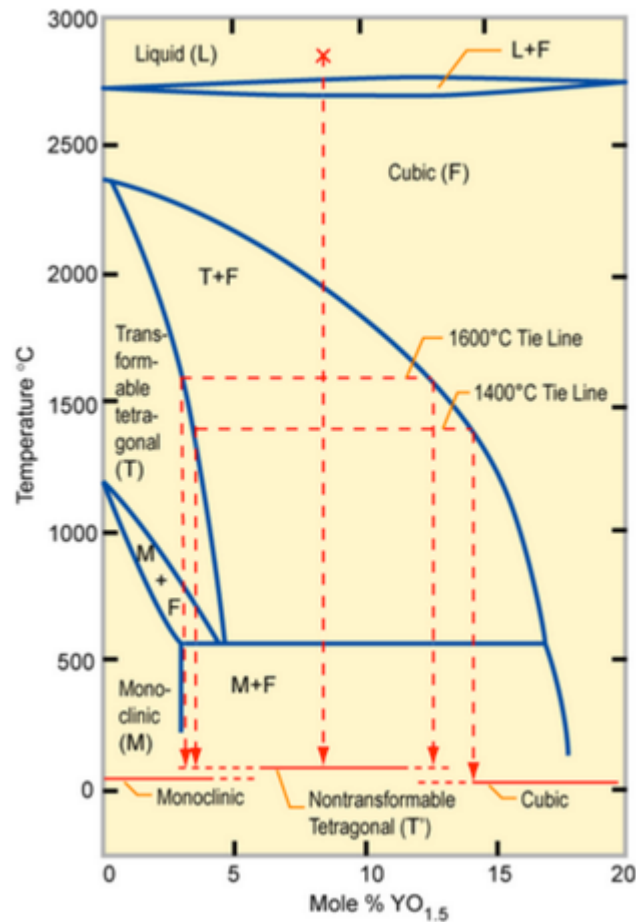


Figure 2.2: YSZ phase diagram showing the phase dependence on yttria dopant percentage and temperature.

Although 3mol% YSZ is usually used in applications requiring its strength and hardness, it is also used as a solid oxide fuel cell (SOFC) solid-state electrolyte. It still has a lower conductivity than 8mol%, which has been shown to produce the best ionic conduction[30,31]. The ionic conductivity increases with the dopant concentration up to 8-9 mol% yttria, and then is reduced

by the addition of more dopant 9+mol%, even though there are more vacancies for oxygen to diffuse. [32-34]. Some of the possibilities proposed for this decrease are defect interactions, clustering effects and the tendency of atomic ordering. The addition of yttria could create more Coulomb attraction between dopant cations (i.e., Y) and oxygen vacancies, trapping the vacancies in defect complexes resulting in decreased conductivity [35,36]. The interest in how oxygen conducts through the unit cell might be elucidated by a high-pressure structural study. The only static high-pressure study on YSZ is a single crystal high pressure Raman spectroscopy study that went up to 6GPa [38]. The paper found that there was a slow phase transition for the 3mol% single crystal, from monoclinic ($P2_{1/b}$) to tetragonal ($P4_{2/nmc}$) above 4.2GPa, and it was irreversible. The 8mol% single crystal was observed to be in the tetragonal ($P4_{2/nmc}$) space group at ambient conditions and did not have a phase transition over the applied pressure range. There has also been a paper published on laser shocked 3mol% YSZ in pressure ranges of 0-10GPa [39]. To the best of this author's knowledge, there has not been a high-pressure impedance spectroscopy study performed on YSZ. The information learned from this type of experiment could help answer some of the puzzling questions that scientists have pertaining to the conduction pathways of YSZ.

CHAPTER 3

General Theory

The general theory of the experimental techniques implemented in this experiment will be discussed, along with references to the source material describing these processes in much more detail.

IMPEDANCE SPECTROSCOPY

Electrical impedance spectroscopy (EIS) has recently become an invaluable tool, used by industry and academia to characterize materials quickly and accurately. Electrical conductivity can be measured in two forms as DC and AC conductivity; the latter being a much more illuminating property that can shine laser light on the microstructure and transport capabilities of a material. AC techniques are used to measure material properties such as ionic/electron transport, bulk conductivity, activation energy, grain boundary, surface, interface, corrosion, diffusion effects, capacitive relaxations, interfacial reactions, redox reactions, and evolving microstructures [39]. EIS can study the influence of an external stimulus on the conductivity of an electrode-electrolyte system. From the impedance spectrum, one can derive electrolyte properties such as conductivity, bulk generation recombination rates, equilibrium concentration of the charged species, mobility of charges, and dielectric constant, as well as, capacitance of the interface region, adsorbed reaction rate constants, diffusion coefficients of species in the electrode relating to the electrode-electrolyte interface [41,42,43]. In 1969, Bauerle was the first to use EIS to study solid-state electrolytes. Since then investigations into single and polycrystalline materials with EIS has only increased, especially because of the desire to create solid-state batteries and more efficient fuel cells [43].

Impedance spectroscopy is only one component of a broader topic called *immitance spectroscopy*, which includes the admittance (Y), dielectric (ϵ), modulus (M), and impedance (Z) functions. The complex dielectric constant defined as $\epsilon^* = \epsilon' - i\epsilon''$. Where ϵ' is the real or relative permittivity or dielectric constant and ϵ'' is the imaginary or dielectric loss of a material. The complex modulus is defined as $M^* = M' + iM''$ and represents a measure of distribution ion energies or configurations in a materials' structure. The complex admittance is the reciprocal of the impedance [40]. In Table 3.1 the relationship between the four components is shown and each function is generally represented as a complex number.

Table 3.1.1 Relations Between Immitance Functions

	M	Z	Y	ϵ
M	M	μZ	μY^{-1}	ϵ^{-1}
Z	$\mu^{-1} M$	Z	Y^{-1}	$\mu^{-1} \epsilon^{-1}$
Y	μM^{-1}	Z^{-1}	Y	$\mu \epsilon$
ϵ	M^{-1}	$\mu^{-1} Z^{-1}$	$M^{-1} Y$	ϵ

$\mu = j\omega C_c$, where C_c is the capacitance of the empty cell

Depending on what characteristic one is interested in learning about a material, one of the specific functions described above must be measured. For instance, to examine the dielectric nature of a material, then the dielectric and modulus spectrum is measured. If concerned with the ionic transport/conductivity of a material, they would want to measure the impedance and admittance.

Impedance is described as the quotient of a voltage and current calculated from a small single sinusoidal measurement. When an AC signal is applied to a system, the impedance of the system obeys Ohm's law as the ratio of voltage to current in the time domain [4]. A small

sinusoidal voltage is applied to the sample and a current response is recorded, giving an impedance that is a complex quantity with a magnitude $|Z|$ and phase shift θ .

$$Z = \frac{V}{I} = \frac{V_o \sin(\omega t)}{I_o \sin(\omega t + \theta)} = Z_o \frac{V_o e^{j\omega t}}{I_o e^{j(\omega t - \theta)}} \quad 3.1$$

The impedance can be simplified to:

$$Z(\omega) = \frac{V}{I} = Z_o e^{j\theta} = Z_o (\cos\theta + j\sin\theta) \quad 3.2$$

$$Z^* = Z' - jZ'' \quad 3.3$$

The complex impedance can then be written in terms of its real and imaginary components in rectangular coordinates:

$$\begin{aligned} \text{Re}Z(\omega) &= Z' = Z \cos\theta \\ \text{Im}Z(\omega) &= Z'' = Z \sin\theta \end{aligned} \quad 3.4$$

Notice above, that the impedance is dependent on frequency and is time invariant. In practice, this is because each time the current response is measured, the oscillating voltage is at a specific, known frequency. Most electrode/electrolyte systems are electrically nonlinear systems, but if a small enough signal is applied ($<500\text{mV}$), then linear AC circuit theory can be applied as seen above.

A simplistic experimental schematic is shown in Figure 3.1. Usually in solid-state EIS experiments, two electrodes are attached to either side of a sample. Then, a small sinusoidal voltage is applied and the current response is measured. The electrodes used need to be highly conducting metal, but also to prevent the mobile ions in the sample material from jumping the electrode sample interface. This is to ensure that none of the ions diffuse into or react with the electrodes, allowing the sample to remain stable and reproduce similar results over time. In other types of experiments, corrosion and diffusion effects are investigated, thus different electrodes

and configurations are used. Additionally, most EIS investigations aim to obtain data as a function of temperature, so most samples are surrounded by heaters/cryostats, thermocouples, insulators, and temperature controllers. In the next section, the experimental setup and how different temperature conditions were achieved will be discussed.

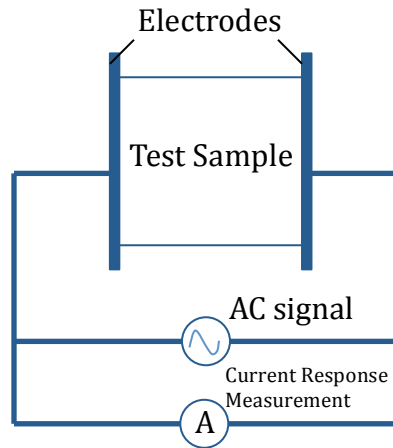
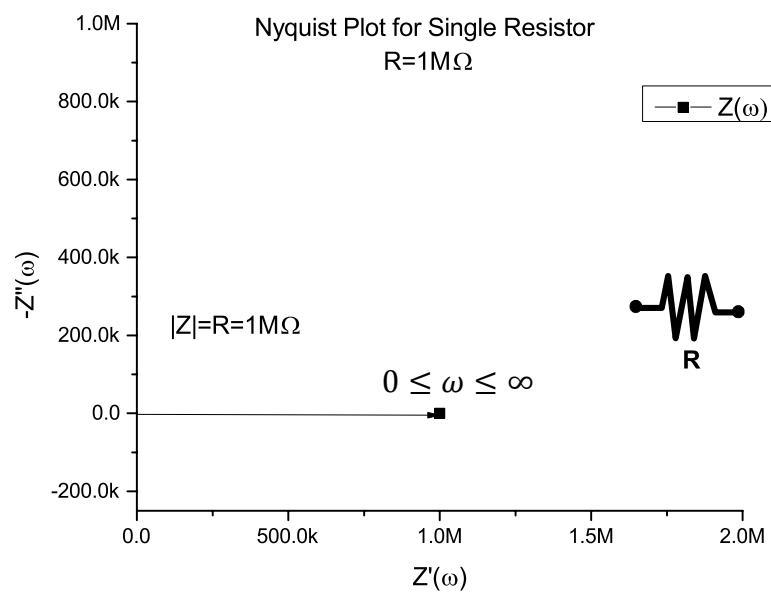


Figure 3.1: Simple Schematic for basic EIS measurement

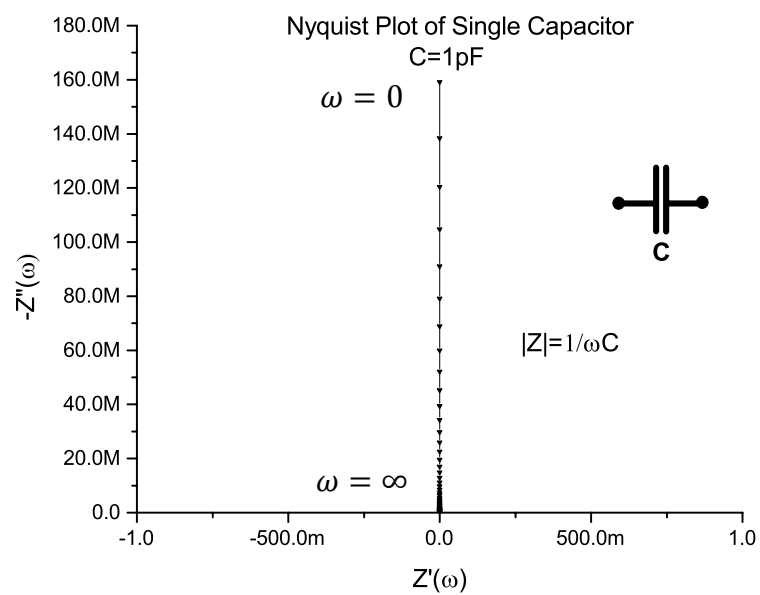
The usual data representation of the impedance spectrum is with either a Bode plot or a Nyquist plot. In a Bode plot, the impedance and phase are plotted together as a function of $\log(f)$. In a Nyquist plot, the real and imaginary parts of the impedance are plotted parametrically with ω . The real part represents the resistance, R , of the impedance and is plotted on the abscissa, where as, the imaginary part or the reactance, X , is plotted on the ordinate. Due to the fact that the reactance is usually negative, the $-X$ is plotted to represent the impedance in the first quadrant.

Materials such as semiconductors, ionic conductors, dielectrics, mixed ionic-electric conductors, and electronic conductors at specific temperatures, each have unique impedance

spectra. The impedance profile of the material can be modeled/represented by a *common equivalent circuit*. These circuits are made up of ideal lump components like resistors, capacitors, and inductors. For example, placing a dielectric in the setup shown in Figure 3.1 and measuring the impedance spectrum, one will see purely capacitive behavior. Likewise, if one performs EIS on an electrical conductor, the impedance spectrum will show the profile of a resistor. In Figure 3.2 the impedance spectrum of a pure capacitor and resistor are shown on a Nyquist Plot, along with their equivalent circuit. For a pure conductor or resistor, its impedance is represented as a single point because it is frequency independent, remembering that the impedance of a resistor is $|Z_R|=R$. Similarly, the following the equation for the impedance of a capacitor, $|Z_C|=1/\omega C$, the impedance will limit to zero as the frequency goes to infinity and become a short circuit



(a)



(b)

Figure 3.2 Nyquist Plot for (a)resistor and (b)capacitor

In Figure 3.3, a Nyquist plot for a series combination of a resistor and capacitor is displayed. There are many different combinations of ideal circuit components that can be added together in different configurations to match experimental data.

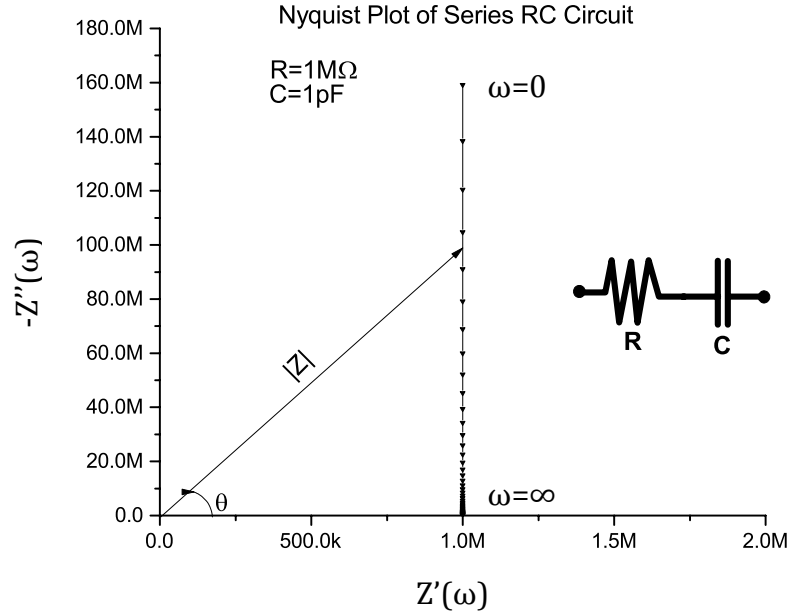


Figure 3.3: Nyquist plot of resistor and capacitor in series

A more complicated impedance profile, a parallel combination of a resistor and capacitor, is represented as a Bode plot and Nyquist plot in Figure 3.4. The semicircular behavior seen is usually observed in solid-state ionic conductors [40]. The semicircle represents a physical relaxation process in the sample material and the time constant of the circuit can be calculated by taking the inverse of the frequency at the apex of the semicircle and setting it equal to the RC time constant, $\omega^{-1} = \tau = RC$. Multiple semicircles can appear on an impedance spectrum, each relating to a different physical process. If the time constants of these physical phenomena are similar, they can overlap and create one large semicircle.

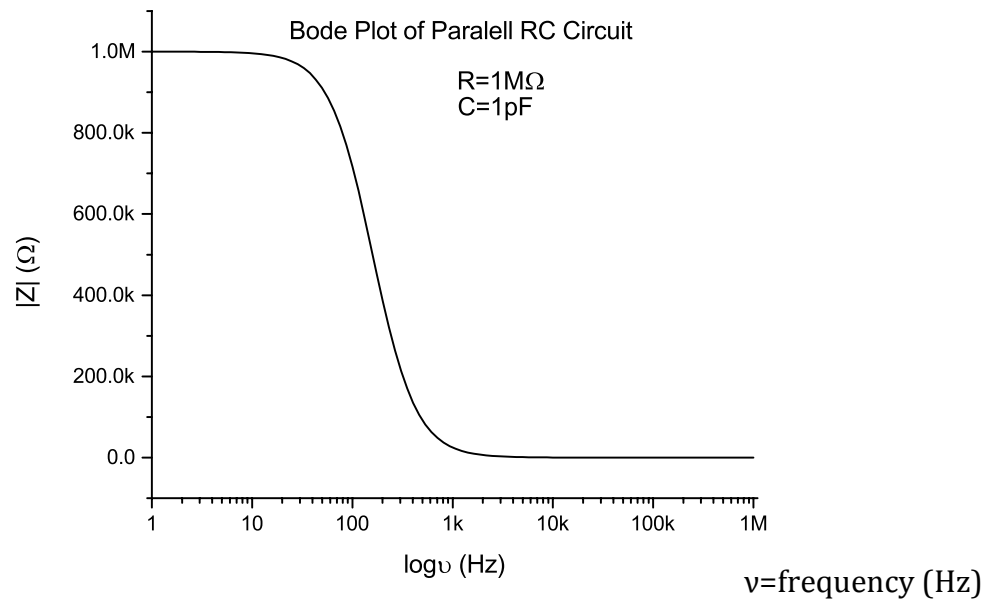
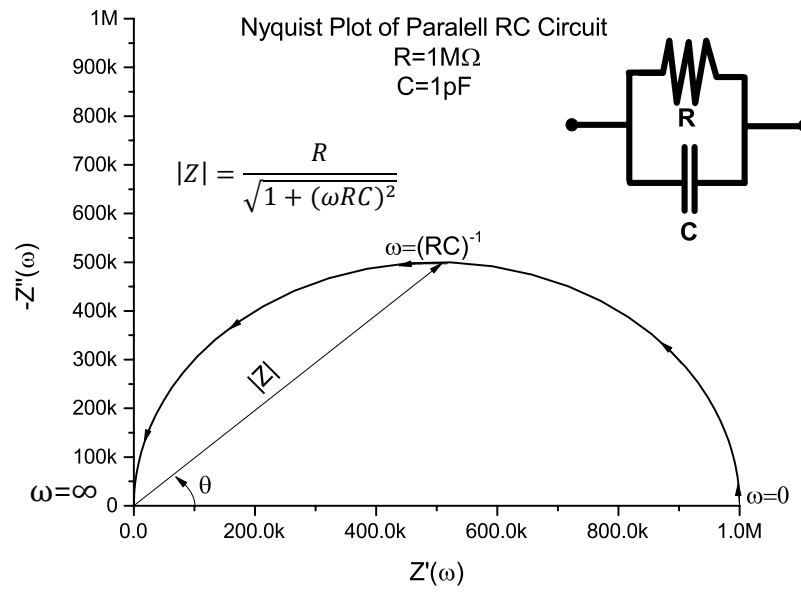


Figure 3.4: (a) Nyquist plot of parallel RC circuit. (b) Bode plot of RC circuit

Some of the drawbacks of using equivalent circuits to model impedance behavior, are that multiple circuits can fit experimental data. In a homogenous sample material, such as a highly pure single crystal with blocking electrodes, the impedance spectrum will look similar to Figure 3.4, but the equivalent circuit will be modified to meet the specific geometric parameters of the sample [44,45] shown in Figure 3.5.

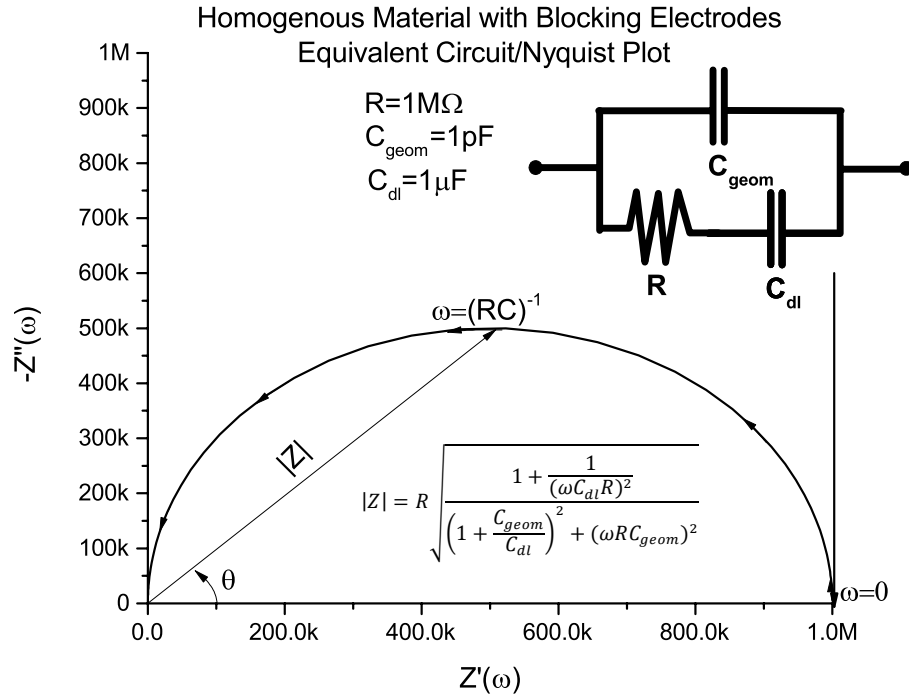


Figure 3.5: Nyquist plot and circuit for a homogenous material with blocking electrodes. The double layer capacitance caused by the two electrodes is combined into one capacitor labeled C_{dl} . C_{geom} is the capacitance of the material and R is the ionic resistance of the material [40].

Single crystal samples can be much harder and more costly to work with, thus most experiments investigate polycrystalline sample material. Due to the fact that polycrystalline sample is made up of many grains; different profiles can be observed in the impedance spectrum. Figure 3.6 shows a modified model proposed by Brauerle (1969)[46], to describe polycrystalline yttria stabilized zirconia, which uses a semicircle for the impedance of the grain interior (bulk), grain boundary, and electrode/electrolyte interface. This impedance spectrum can be modeled as three

parallel circuits in series. A single crystal sample does not have a grain boundary resistance due to its homogenous nature [40].

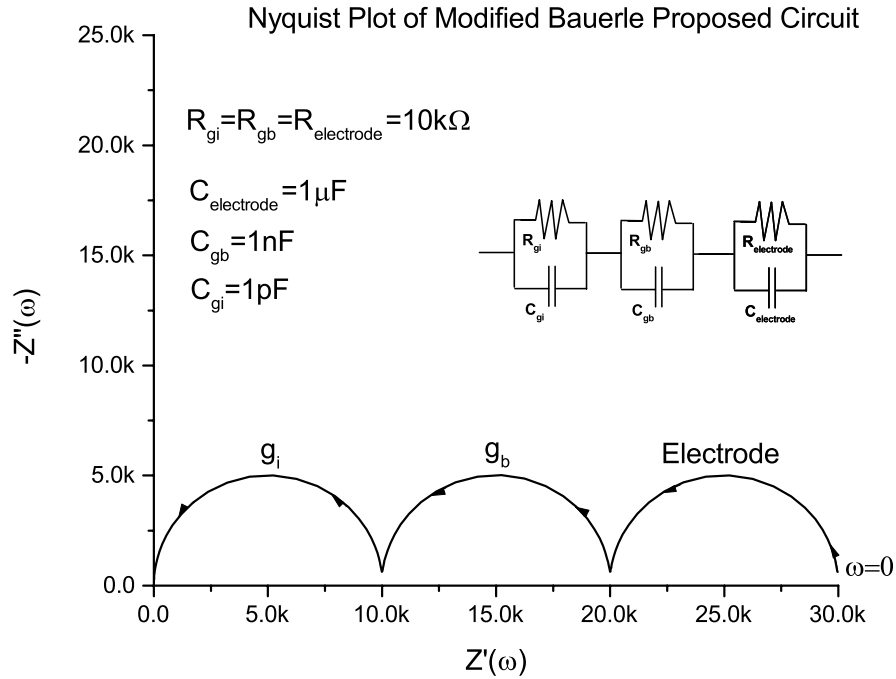


Figure 3.6: The Nyquist plot and equivalent circuit for the Modified Bauerle proposed circuit.

A simple way to represent EIS measurements on polycrystalline sample is the *Brick Layer Model* [47,48], which is shown in Figure 3.7. Although a polycrystalline sample has many inhomogeneities, such as a varying time constant over sample grains, different grain compositions, sizes and orientations, the brick layer model gives a good qualitative picture of how the material behaves on average. The brick model is quite simplified; many more complex processes can occur at the electrode/electrolyte interface. If the electrodes being used are completely blocking, then the semicircle displayed in Figure 3.6 (labeled electrode) would instead be a straight line because the electrode would act as a pure capacitor.

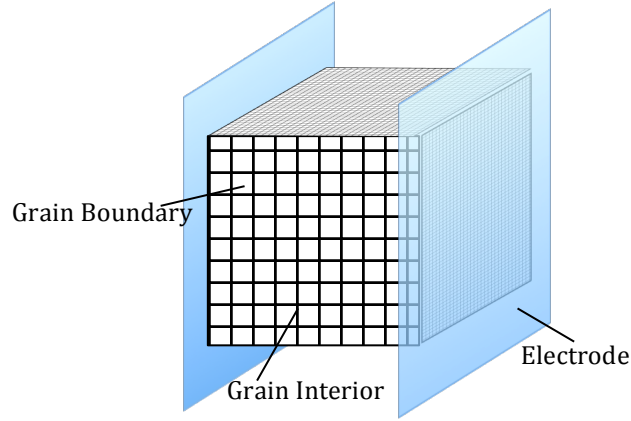


Figure 3.7: Brick Layer Model

If some of the mobile ions were able to diffuse into the electrode, then, at low frequency, there would be an angled tail that can be described by *Warburg diffusion*. Additionally, other profiles can be seen in the impedance spectrum from polarization and charge transfer resistance [40].

The Kramers-Kronig relations between imaginary and real impedance is another useful tool provided by EIS. One can calculate the real impedance from the imaginary or vice versa from a linear response function. The relationship can be expressed as:

$$Z'(\omega) = \frac{2}{\pi} P \int_0^{\infty} \frac{\omega' Z''}{\omega'^2 - \omega^2} d\omega' \quad 3.5$$

$$Z''(\omega) = \frac{2\omega}{\pi} P \int_0^{\infty} \frac{\omega' Z'}{\omega'^2 - \omega^2} d\omega' \quad 3.6$$

Where the P (principal value) indicates that the integration excludes the point $\omega' = \omega$. The KK relation, owing to the KK transforms' stability and causality, can determine the validity of experimental data. When applying the KK transform to data, the integration occurs over a finite frequency range and if the system is unstable, changing in time, the KK relation will not be satisfied.

After impedance spectra are obtained, the experimental resistance of the bulk (grain interior) and grain boundary resistance can be determined from the semicircular arcs. By knowing the sample material geometry, one can then use the following equation to calculate the resistivity and conductivity of the sample.

$$\rho = R \frac{A}{l} \quad 3.7$$

$$\sigma = \rho^{-1} = \frac{l}{RA} \quad 3.8$$

Where R is the resistance, A is the cross sectional area, l is the length or in case of this experiment, the thickness of the sample, ρ is the resistivity of the sample, and σ is the conductivity. Often in EIS experiments, due to the inhomogeneity of the sample, the center of the semicircles formed are below the abscissa axis. To obtain a reliable fit on impedance spectroscopy data with this problem, a *constant phase element* is used [49]. Represented as Q , its relation to the impedance is given below:

$$|Z_Q| = \frac{1}{Q\omega^\alpha} \quad 3.9$$

α is the angle from the origin to the center of the semicircle. Q basically is an effective capacitance for a non-homogenous system.

RUBY FLUORESCENCE

Currently, there are multiple ways to measure pressure in a diamond anvil experiment (DAC), one of the most popular being *ruby fluorescence*. This technique was developed by *Mao et al*, in 1978, and later corrected by *Mao et al*, in 1985 [50]. Additionally, other papers have been published discussing the pressure calibration of ruby at different thermal conditions [51].

When photons are incident on ruby, $\text{Al}_2\text{O}_3: \text{Cr}^{3+}$, the electrons in the Cr^{3+} ground state are excited to states E_3 and E_4 and then rapidly make a non-radiative transition into a long lived metastable state E_2 , as seen in figure 3.8. Spin splitting creates two long-lived energy levels in the E_2 meta-stable state. The R_1 and R_2 emission peaks are created when the excited electrons in the E_2 state transition back to their ground state and emit photons; the photon emitted from the higher E_2 energy state is the R_1 line in the ruby spectrum, where as the lower energy E_2 state produces the R_2 line.

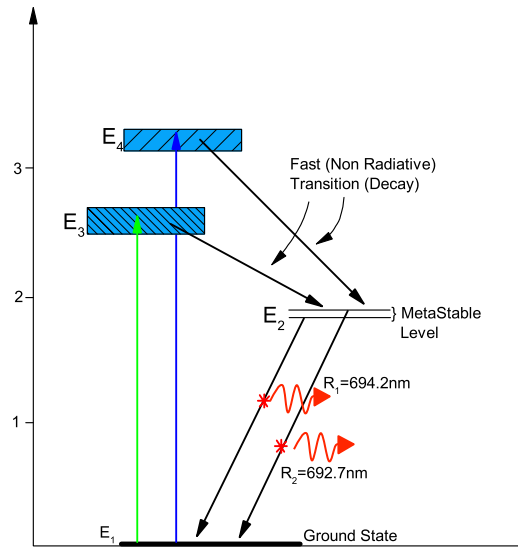


Figure 3.8: Energy Level Diagram for fluorescence of ruby.

As pressure is applied to the ruby, the difference between energy levels in E_2 evolves in a well-understood manner. When the ruby fluoresces, usually from focused laser light, the wavelengths of the emitted photons can be measured, and the pressure determined. In figure 3.9, an example of the ruby fluorescence spectrum is shown at ambient pressure and at 12GPa, notice, R_1 is a longer wavelength than R_2 .

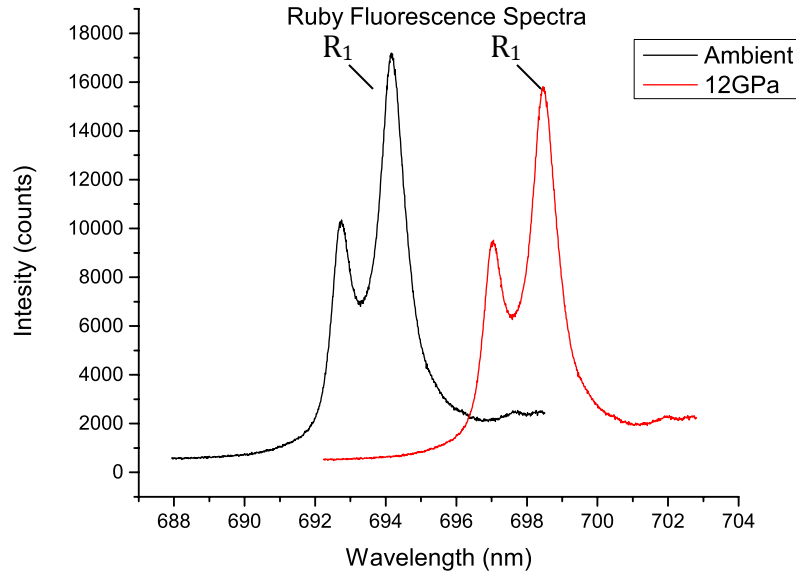


Figure 3.9: Ruby spectra at ambient pressure and at 12GPa. Notice the R_1 peak shift with pressure.

In the [50] paper, an equation was given, using the shift of the R_1 line from ambient pressure, to calculate pressure.

$$P(\text{GPa}) = 380.8 \left(\left(\frac{\lambda}{694.2} \right)^5 - 1 \right) \quad 3.10$$

λ is the peak position of the R_1 line. If 694.2 is substituted in for λ , the pressure calculated is 0GPa. As can be seen in figure 3.9, the R_1 peak under ambient pressure is at 694.2nm. Also, if

the wavelength of the R_1 line of the 12GPa spectrum, 700nm, is inserted into Equation 3.10 a pressure of 12GPa is calculated.

The ruby spectrum can also be a good determination of how hydrostatic the pressure conditions the system being measured is under. As higher pressures are attained, the ruby spectrum peaks will usually broaden, depending on the sample and pressure transmitting medium being used. As non-hydrostatic conditions develop, the R_1 and R_2 peaks become very broad and cannot be resolved.

POWDER X-RAY DIFFRACTION

Advances in x-ray diffraction techniques techniques have allowed fine powders to be characterized [53,54]. The basic principles of XRD rely on the interaction of x-ray photons interacting with atomic electrons and scattering elastically in all directions. A fraction of the x-ray photons incident on crystal, will specularly reflect off of the parallel planes of atoms. At certain angles, the scattered x-rays will constructively interfere. A *diffraction*, plots the intensity of photons measured versus the scattering angle. The position of diffraction peaks depends on the constructive interference condition, also known as *Bragg's Law*, given in equation 3.11.

$$2d\sin\theta = n\lambda \quad 3.11$$

λ is the wavelength of the incident x-rays, θ is the angle that photons diffract off of the lattice planes, and d is the space between atomic planes.

The crystal lattice that the x-rays diffract from can be described by a mathematical set of fixed points in a particular arrangement. Each point in the lattice can have a group of atoms attached to it, which is defined as a basis. In an ideal crystal, infinite repetitions of the basis are

attached to the lattice. The lattice can be described by three translation vectors \mathbf{a}_1 , \mathbf{a}_2 , and \mathbf{a}_3 , so that the crystal will look the same at any point in coordinate space. Equation 3.12 gives the description of the crystal under a translation from a point \mathbf{r} to a point \mathbf{r}' . It should be noted that the crystal can be translated to a different point, but the translation vectors are unchanged.

$$\mathbf{r}' = \mathbf{r} + u_1\mathbf{a}_1 + u_2\mathbf{a}_2 + u_3\mathbf{a}_3 \quad 3.12$$

\mathbf{r}' is the translated point from \mathbf{r} and u_1, u_2 , and u_3 are integers. Periodicity of the lattice can control many physical processes. So to fully understand a material, a fundamental understanding of the crystal lattice is essential [55].

Depending on the symmetry of the crystal and the arrangement of lattice points, can be categorized into one of seven cells being cubic, trigonal, hexagonal, tetragonal, orthorhombic, monoclinic, and triclinic systems [56]. The most general system is triclinic, where none of the primitive vectors and angles equals each other, $\mathbf{a} \neq \mathbf{b} \neq \mathbf{c}$ and $\alpha \neq \beta \neq \gamma$. In Table 3.1 a list of the seven possible systems and the number of lattice systems they contain is shown. For example, the cubic system can have a simple cubic, base-centered cubic, and face centered cubic lattice.

Table 3.3.1 *Bravais Lattices*

System	Number of Lattices	Restrictions on conventional cell axes and angles
Triclinic	1	$\mathbf{a} \neq \mathbf{b} \neq \mathbf{c}$ and $\alpha \neq \beta \neq \gamma$
Monoclinic	2	$\mathbf{a} \neq \mathbf{b} \neq \mathbf{c}$ and $\alpha = \gamma = 90^\circ \neq \beta$
Orthorhombic	4	$\mathbf{a} \neq \mathbf{b} \neq \mathbf{c}$ and $\alpha = \gamma = \beta = 90^\circ$
Tetragonal	2	$\mathbf{a} = \mathbf{b} \neq \mathbf{c}$ and $\alpha = \gamma = \beta = 90^\circ$
Cubic	3	$\mathbf{a} = \mathbf{b} = \mathbf{c}$ and $\alpha = \gamma = \beta = 90^\circ$
Hexagonal	1	$\mathbf{a} = \mathbf{b} \neq \mathbf{c}$ and $\alpha = \beta = 90^\circ$, $\gamma = 120^\circ$
Trigonal	1	$\mathbf{a} = \mathbf{b} = \mathbf{c}$ and $\alpha = \gamma = \beta < 120^\circ$

All 14 possible lattice types in three dimensions [55]

XRD data is usually imported into auto-indexing programs to determine the lattice structure of a material [57] With reasonable initial starting parameters one can describe the structure of a sample confidently.

CHAPTER 4

EXPERIMENTAL SETUP

In the experimental section, the experimental setup will be discussed, along with diagrams and pictures of the equipment used.

SAMPLE MATERIAL

The 3 and 8mol% YSZ powder were purchased from Inframat Advanced Materials and Sigma Aldrich respectively. The grain size was $<1\mu\text{m}$. The samples were 99.9% $\text{Y}_2\text{O}_3 + \text{ZrO}_2$, with a contamination of $<0.1\%\text{HfO}_2$. The samples were characterized by XRD taken on a Bruker D8 X-ray Diffraction Machine® over a two-theta range of 5° to 80° . The x-ray wavelength was 1.54\AA (Cu $K\alpha$). The pattern collected was compared to a generated pattern, simulated with PowderCell® software and cell parameters given in literature. The simulated pattern and measured pattern matched with good agreement.

HIGH-PRESSURE IMPEDANCE SPECTROSCOPY

The high-pressure impedance spectroscopy study of 3, 8mol% YSZ occurred in a Merrill-Bassett type diamond anvil cell. The impedance spectra were measured with a Solatron 1260 Impedance Gain Phase Analyzer® at pressures of 0-17GPa and at temperatures of 294-523K.

DIAMOND ANVIL CELL

The diamond anvil cell used was a Merrill-Bassett type DAC, with 500um cutlets glued with high temperature epoxy. Figure 4.1 shows the DAC open and loaded below.



Figure 4.1 Merrill-Bassett type diamond anvil cell (DAC) closed on the left, open on the right.

NON-CONDUCTIVE GASKET

A non-conductive gasket was created using a stainless steel (SS) gasket that was pre-indented to 50um. The entire center of the pre-indentation was drilled out using the laser-drilling machine at the High Pressure Collaborative Access Team (HP-CAT) Sector 16 located at the Advanced Photon Source (APS) at Argonne National Laboratory (ANL). An epoxy mix of 10:1, by weight, c-BN powder, purchased from Advanced Abrasives®, mixed with EPO-TEC 253® High Temperature epoxy and isopropanol, to create a good mix, was cooked at 100°C for 12 hours to allowing the epoxy to set. After this, a small amount of the mix was compressed into the hole of the drilled SS gasket and was compressed to 20GPa in the Merrell-Bassett DAC. Next Stycast 2850® was painted on either side of the stainless steel gasket to create a non-conducting surface. Next, the compressed painted non-conductive gasket was drilled manually to produce a 280um diameter hole for the sample material. Platinum foil, 20um thick, was then cut to create to

leads for the impedance spectroscopy measurement. Care was taken to ensure the leads were the same size of $\sim 50\mu\text{m}$. The sample material was packed into the sample hole and platinum leads were sandwiched on top and bottom of the sample, making sure to align the leads directly over each other. Copper wire was then glued onto the Pt leads with Emerson & Cummings® Silver Epoxy. The gasket was then heated at 75°C for 24hrs to allow the silver epoxy to set. To finish the loading, a ruby was placed on a non-covered part of the sample to be the pressure marker.

Figure 4.2. shows a diagram of the setup.

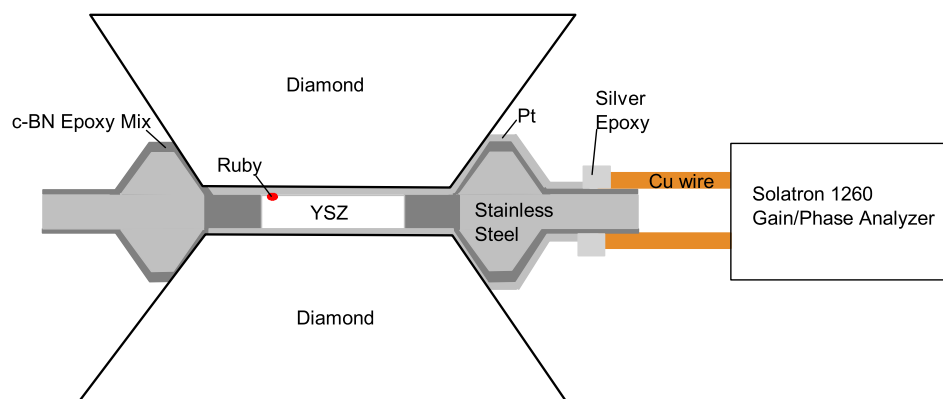


Figure 4.2: Non-conductive Gasket set up

A 514.5nm laser was used to excite ruby. A Jobin Yvon U1000® Spectrometer and an ISA Instruments Spectrum One® detector collected and measured the emission lines. Using Winspec® software the peak position of the R_1 line was determined. Pressures were characterized by this method before each impedance spectroscopy measurement. Figure 4.3 shows the gasket before heating and pressuring.

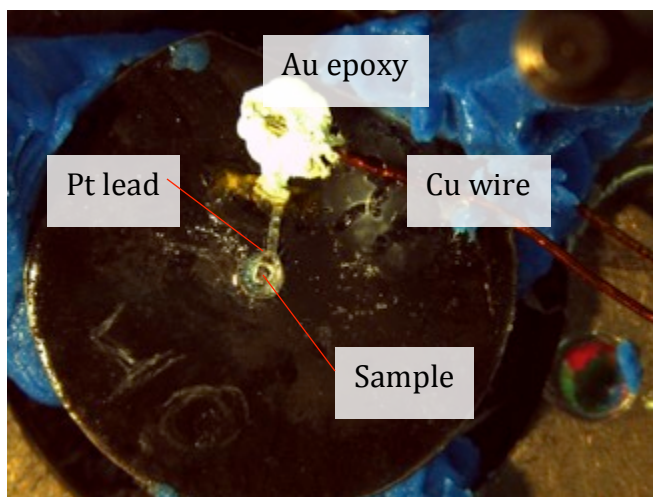
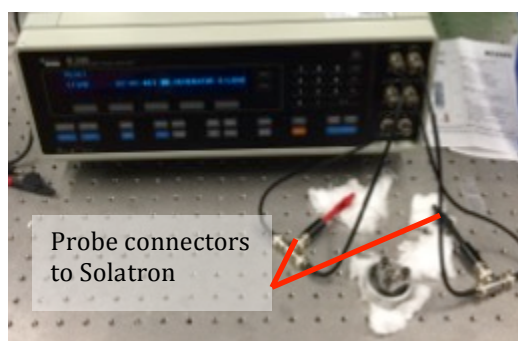
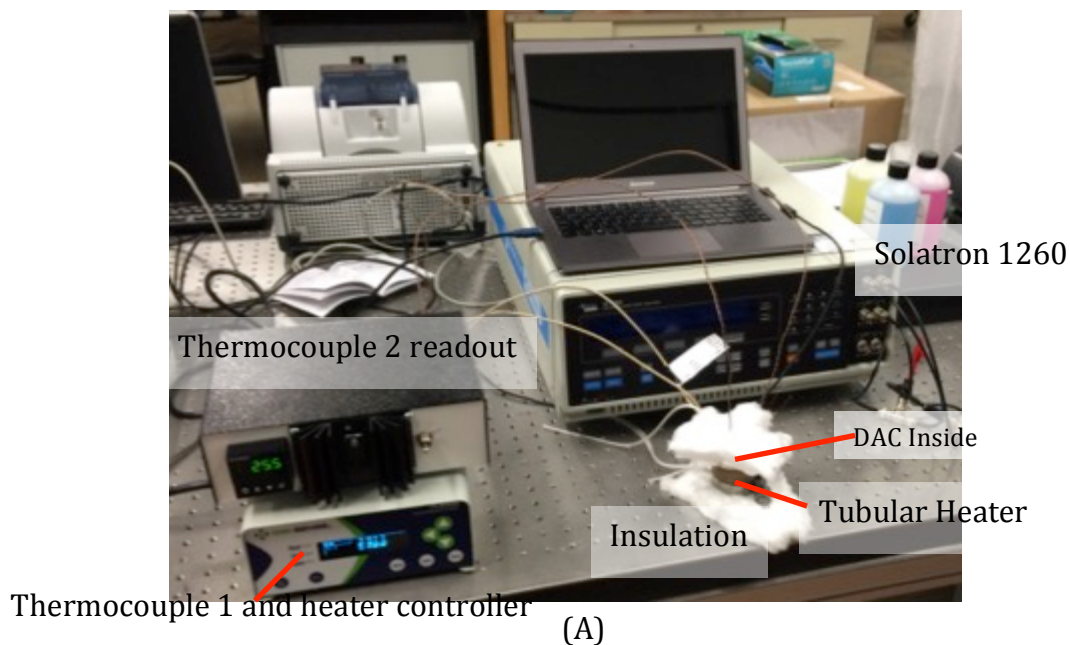


Figure 4.3 Picture of the nonconductive gasket loaded with sample.

IMPEDANCE MEASUREMENT

Two trials were performed, one for the 3mol% YSZ and one for the 8mol% YSZ. The DAC once loaded and the pressure determined, was placed inside an oven, with a thermocouple attached to the bottom and top of the DAC. The two copper wires attached to the Pt lead were then connected to the Solatron 1260 Impedance Gain/Phase Analyzer®. The heater was programmed to heat the sample up to 250°C at 5°C/minute. Once the maximum temperature was obtained, the sample was allowed to cool and thermalize for 10 minutes at 250°C, 190°C, 140°C, and 100°C. After a 10 minute wait time, the impedance spectrum was measured over a range of 20MHz-1Hz with amplitude of 100mV. SMarT® software, provided by Scribner® (the company that produces the Solatron 1260®) was used to connect to the Solatron®, input test parameters and collect data. Figure 4.4 shows a picture of the setup. After the cell cooled back to ambient temperatures, the DAC was pressured to the next pressurized and the above process, including heating, was repeated.



(B)



(C)

Figure 4.4: (A) Heated impedance spectroscopy with pressure setup. The DAC was inside the oven and its leads connect to the Solatron 1260. (B) A picture of the setup of a non-heated Impedance spectroscopy measurement. (C) The Merrill-Bassett type DAC with copper wires connected to Pt probes.

Once data was collected, it was analyzed with Origin Pro 9.0® software and the Zfit® program running on Matlab® software. The Zfit program was used to simulate common equivalent circuits and fit to the data. In the Results and Discussion section, the fitting process and the functions used to fit the data will be explained.

POWDER X-RAY DIFFRACTION

Powder XRD patterns were taken at the BM-D beam line at HP-CAT Sector 16 at the Advanced Photon Source at Argonne National Laboratory. A Mao-Bell type DAC was used with 500 μm cutlet diamonds, figure 4.5. A stainless steel gasket was pre-indented to 50 μm and a 250 μm hole was drilled with the laser-drilling machine. The first sample studied was 3mol% YSZ, and then a new gasket was made and the 8mol% YSZ was interrogated. The energy of the x-ray beam was 29keV, which converts to the wavelength of 0.4246 \AA and the FWHM of the beam spot was 4.3 μm . A mar345 image plate detector was used to collect the diffraction pattern. Then Dioptas® Software was used to mask and integrate the patterns. Ruby was used as the pressure marker and the offline ruby system at HP-CAT was used to measure pressure. Non-hydrostatic pressures of 0-26 GPa were obtained for both samples. The autoindexing program MDI Jade® was used to fit the XRD data and determine lattice cell parameters.



Figure 4.5 Mao-Bell Type DAC

Chapter 5

RESULTS and DISCUSSION

In this section, the results from the high-pressure impedance spectroscopy experiment and the non-hydrostatic high-pressure powder XRD study for 3 and 8mol% YSZ will be exhibited and discussed

HIGH-PRESSURE IMPEDANCE SPECTROSCOPY RESULTS

Using the experimental setup described in chapter 4, the non-hydrostatic high-pressure impedance spectroscopy measurements were taken at seven pressure points for both samples (3mol% YSZ: 0, 3.1, 6.5, 10.3, 14.2, 16.7, and ~ 5 GPa taken during decompression, 8mol% YSZ: 0, 3.6, 6.1, 10.5, 13.1, 17.5 and ~ 5 GPa during decompression). The impedance was also recorded at four temperatures (100, 140, 190, and 250 $^{\circ}$ C) at each pressure. The applied voltage was 100mV and the frequency varied from 20MHz to 1Hz. The impedance spectrum for each sample is shown below in Figure 5.1 and 5.2. The impedance spectrum for both samples at 100 $^{\circ}$ C and at 140 $^{\circ}$ C can be seen to provide no type of semi circle arc describing conductivity. The vertical nature of the spectrum suggests a totally capacitive behavior. Multiple publications have also found that conductive behavior starts over 150 $^{\circ}$ C [40, 41, 42]. Resistance information could not be interpreted from data at 100 and 140 $^{\circ}$ C. This is because the material does not ionically conduct well at lower temperatures and does not provide a substantial semicircular arc. 190 and 250 $^{\circ}$ C measurements could be used to calculate conductivity because the impedance arcs were well defined.

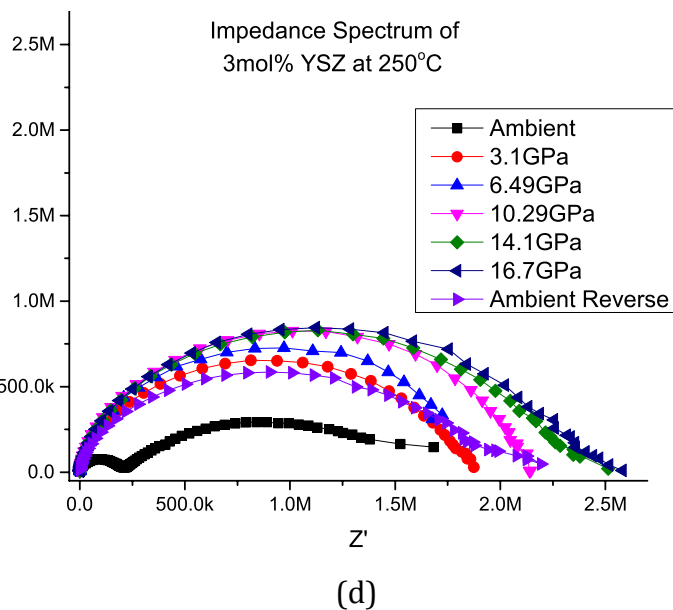
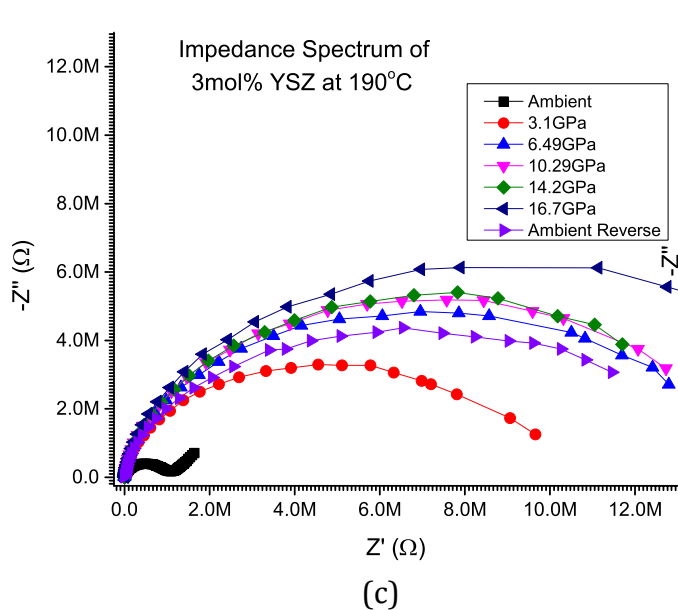
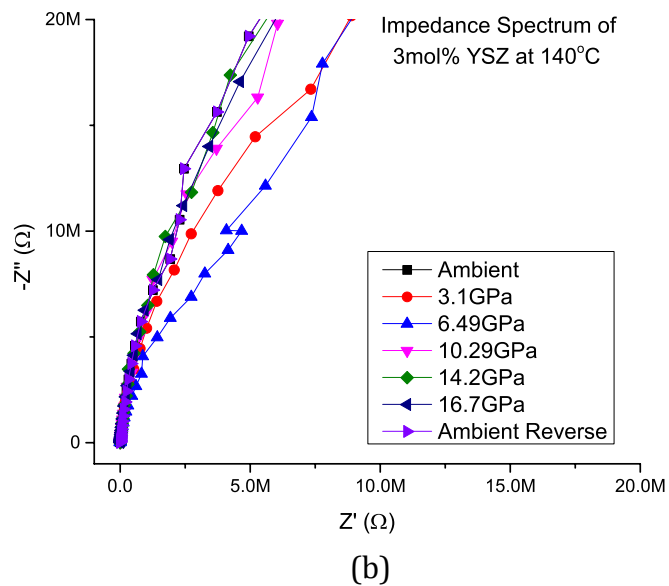
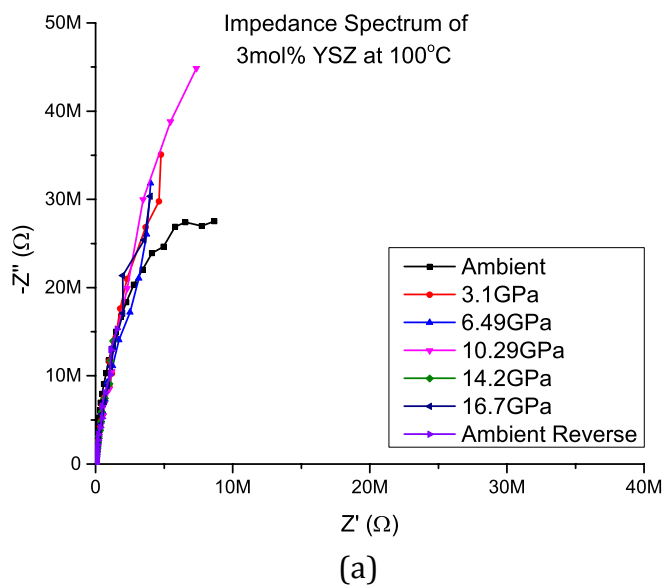


Figure 5.1 Measured impedance spectrum of 3YSZ at (a) 100°C, (b) 140°C, (c) 190°C, (d) 250°C

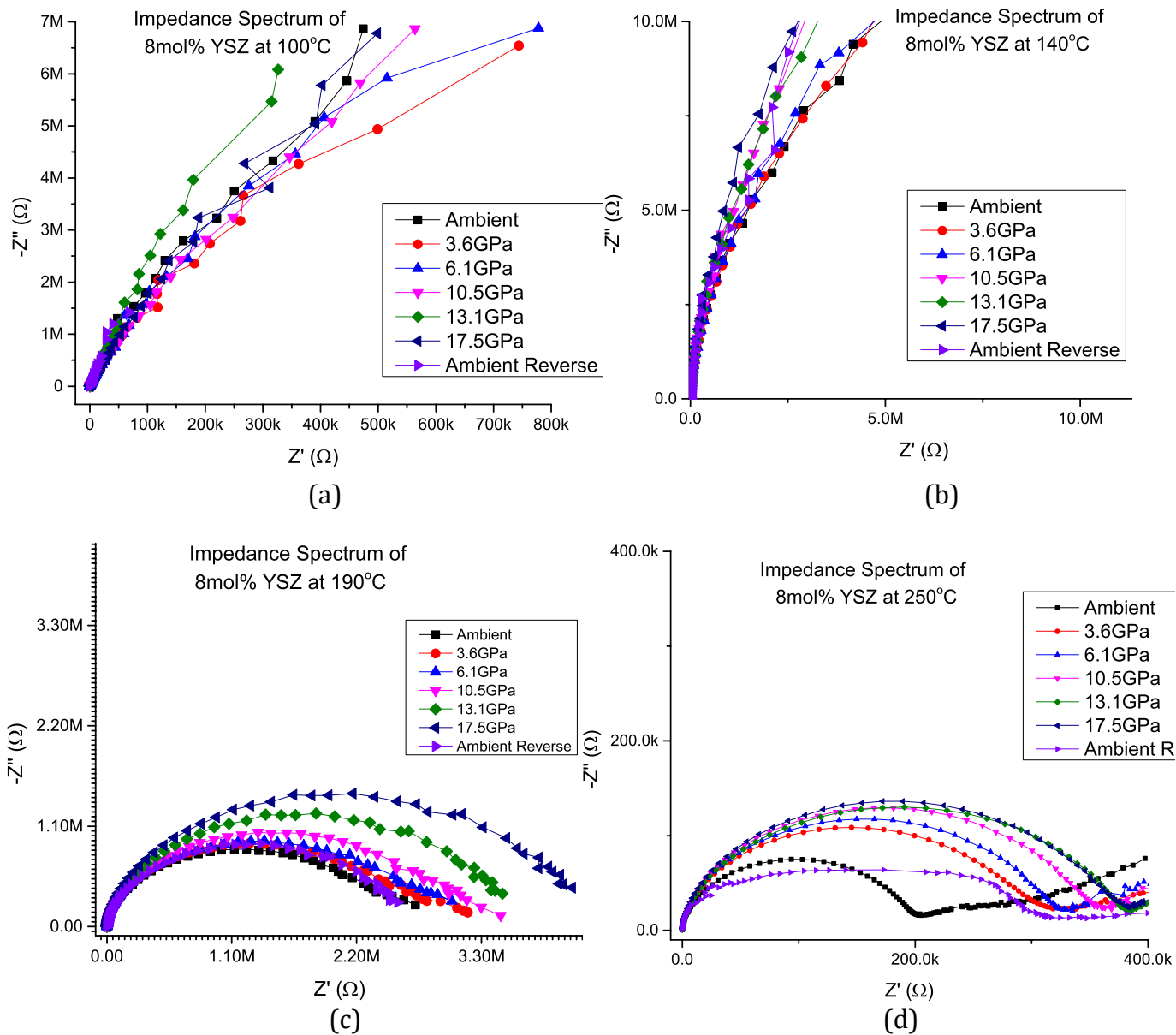


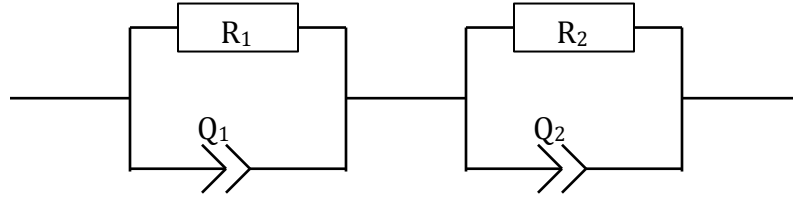
Figure 5.2 Measured impedance spectrum of 8YSZ at (a) 100°C, (b) 140°C, (c) 190°C, (d) 250°C. Note the odd shape of the ambient reverse spectra at 250°C. This could be due to lead damage during decompression to ambient pressures.

For the 3YSZ, the ambient pressure measurements at the higher temperatures display two arcs relating to the internal grain resistance and grain boundary resistance. These arcs have a similar form as data published in [40]. For the ambient spectrum of 8YSZ at 250°C, a clear grain interior arc can be seen, but the grain boundary arc is harder to resolve. Nevertheless, the grain boundary arc can still be fitted and resistance information can be obtained.

As pressure was increased, the grain boundary and grain interior capacitances became similar, resulting in the dip separating the two arcs to disappear at ~3GPa and did not return during decompression. No pressure points were taken between ambient conditions and 3GPa, if there were data points taken in that range, a better understanding of the changing capacitances and resistances could have been made. If more time had been available, impedance spectra would have been measured at more pressure points. The data collected show-increasing diameters of the characteristic arcs with pressure. The diameter of the arc directly represents the resistance of the sample[40], so it can be concluded that with pressure, the resistance of 3 and 8YSZ increases. Also, note the odd shape of the 0GPa decompression spectrum for 8YSZ. This may be from lead damage when opening the DAC.

To determine the resistance values of the measured spectrum, the data was fitted using the equivalent circuit and expressions shown in Figure 5.3. It should be noted that because of the depression of the center of the impedance arcs, a constant phase element, represented as Q , was used to better fit the data. This is a common practice in impedance spectra analysis [40]. Using the equations in Figure 5.3 and the experimental data in the Nyquist plot ($\text{Re}(Z)$ vs $-\text{Im}(Z)$) form, the data can be fitted to determine the resistance of the sample. With knowledge of the geometry and resistance of the sample, one can

Equivalent Circuit Model



$$ReZ(\omega) = \frac{R_1(1 + \omega^{\alpha_1} c_{\alpha_1} \tau_1)}{1 + \omega^{\alpha_1} \tau_1 (2c_{\alpha_1} + \omega^{\alpha_1} \tau_1)} + \frac{R_2(1 + \omega^{\alpha_2} c_{\alpha_2} \tau_2)}{1 + \omega^{\alpha_2} \tau_2 (2c_{\alpha_2} + \omega^{\alpha_2} \tau_2)}$$

$$ImZ(\omega) = -\frac{\omega^{\alpha_1} R_1 s_{\alpha_1} \tau_1}{1 + \omega^{\alpha_1} \tau_1 (2c_{\alpha_1} + \omega^{\alpha_1} \tau_1)} - \frac{\omega^{\alpha_2} R_2 s_{\alpha_2} \tau_2}{1 + \omega^{\alpha_2} \tau_2 (2c_{\alpha_2} + \omega^{\alpha_2} \tau_2)}$$

Where $c_{\alpha_1} = \cos\left(\frac{\pi\alpha}{2}\right)$, $\tau = RQ$, α is an angle making $(1-\alpha)*90$ equal to the angle of depression of impedance arc.

Figure 5.3: The equivalent circuit and function to fit a two-circle impedance spectrum. The R and Q values correspond to the grain interior and grain boundary.

calculate the resistivity and conductivity of the sample using Equation 3.7. In Table 5.1, the determined resistance values, as well as the sample type, temperature, pressure, resistivity, and conductivity are given. Pictures of the sample were taken with a calibrated Leica® Microscope to get the dimensions of the electrode. By knowing the initial thickness and measuring the change in height of the DAC with a micrometer, we determined the thickness of the sample. Additionally, after the completion of the data collection, the sample was measured outside of the DAC to get a better measurement of the final thickness. Even though care was taken to obtain the most accurate thickness measurements, some error is still associated with the values, and was included in the resistivity error value calculations which are presented in Table 5.1. Figures 5.4 and 5.5 display pictures of the samples at different pressures.

Table 5.1: Fitted Resistance and Calculated Conductivity

Sample	Temp. (°C)	Pressure (GPa)	Resistance (MΩ)	Error(R) (10 ⁵ Ω)	ρ-resistivity (kΩ□m)	σ-conductivity (10 ⁻³ S/m)	Error (σ) (10 ⁻⁴ S/m)
3YSZ	250	0	1.43	0.43	0.40	2.52	3.0
		3.1	1.80	0.54	0.58	1.73	2.1
		6.5	1.85	0.55	0.65	1.54	1.8
		10.3	2.05	0.61	0.80	1.27	1.5
		14.2	2.23	0.66	0.92	1.09	1.3
		16.7	2.33	0.70	1.0	0.959	1.2
		0 rev	1.89	0.56	0.85	1.18	1.4
	190	0	4.88	1.5	1.4	0.738	0.89
		3.1	9.23	2.8	2.9	0.335	0.40
		6.5	12.0	3.6	4.3	0.235	0.28
		10.3	13.6	4.1	5.2	0.191	0.23
		14.2	14.1	4.2	5.8	0.173	0.21
		16.7	15.1	4.6	6.8	0.148	0.18
		0 rev	11.4	3.4	5.1	0.197	0.24

Sample	Temp. (°C)	Pressure (GPa)	R (MΩ)	E _R (10 ⁴ Ω)	ρ (10 ² Ω□m)	σ (10 ⁻³ S/m)	E _σ (10 ⁻⁴ S/m)
8YSZ	250	0	0.253	0.76	0.75	14.2	1.7
		3.6	0.402	1.2	1.30	7.69	0.92
		6.1	0.423	1.3	1.49	6.71	0.81
		10.5	0.454	1.4	1.75	5.73	0.69
		13.1	0.495	1.5	2.05	4.89	0.59
		17.5	0.526	1.6	2.35	4.26	0.51
		0 rev	0.391	1.2	1.74	5.75	0.69
	190	0	3.51	8.2	7.62	1.31	0.16
		3.6	4.24	9.3	9.97	1.01	0.12
		6.1	4.51	10.1	11.8	0.845	0.10
		10.5	5.11	11.1	14.2	0.704	0.08
		13.1	5.67	12.3	17.0	0.588	0.07
		17.5	6.09	13.4	19.9	0.503	0.06
		0 rev	4.02	9.1	13.3	0.750	0.09

The resistance values were obtained from fitting the impedance spectroscopy data. The thickness and area of the sample were measured and the resistivity was calculated with Equation 3.7.

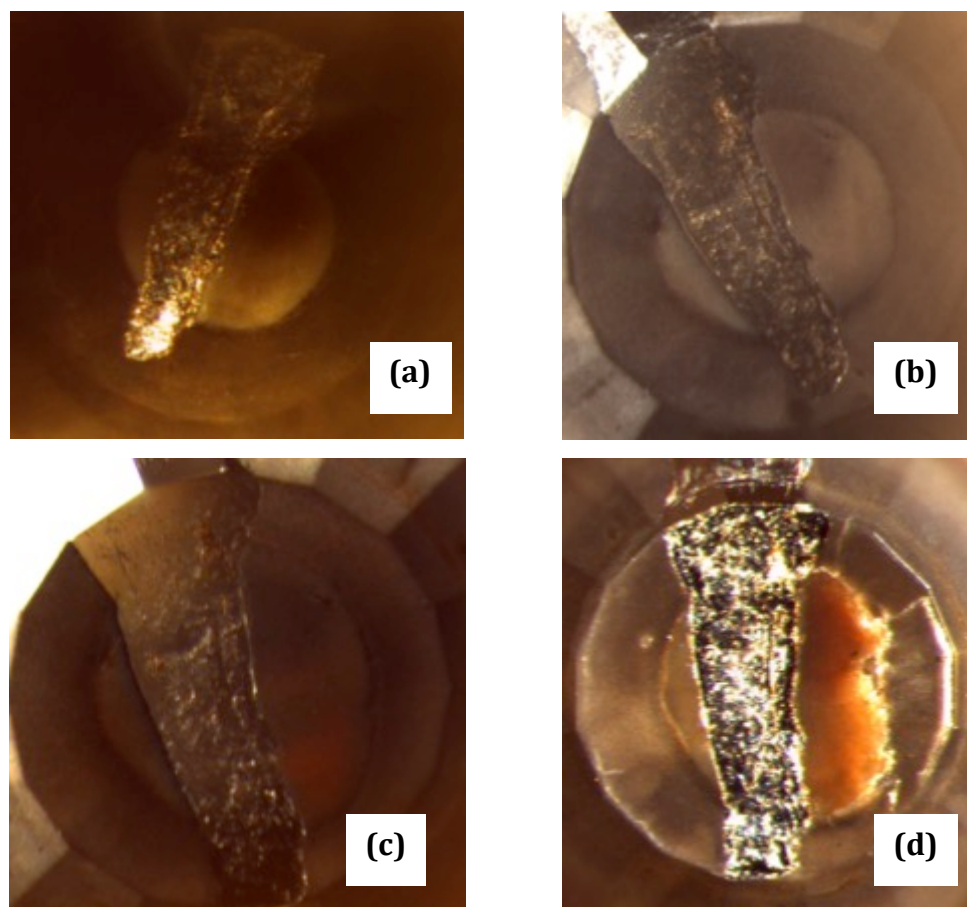


Figure 5.4: 3YSZ sample pictures taken after heating between 25-250°C and at pressures of (a) 0GPa, (b) 6.5GPa, (c) 16.7GPa, (d) 0GPa decompression taken outside of DAC

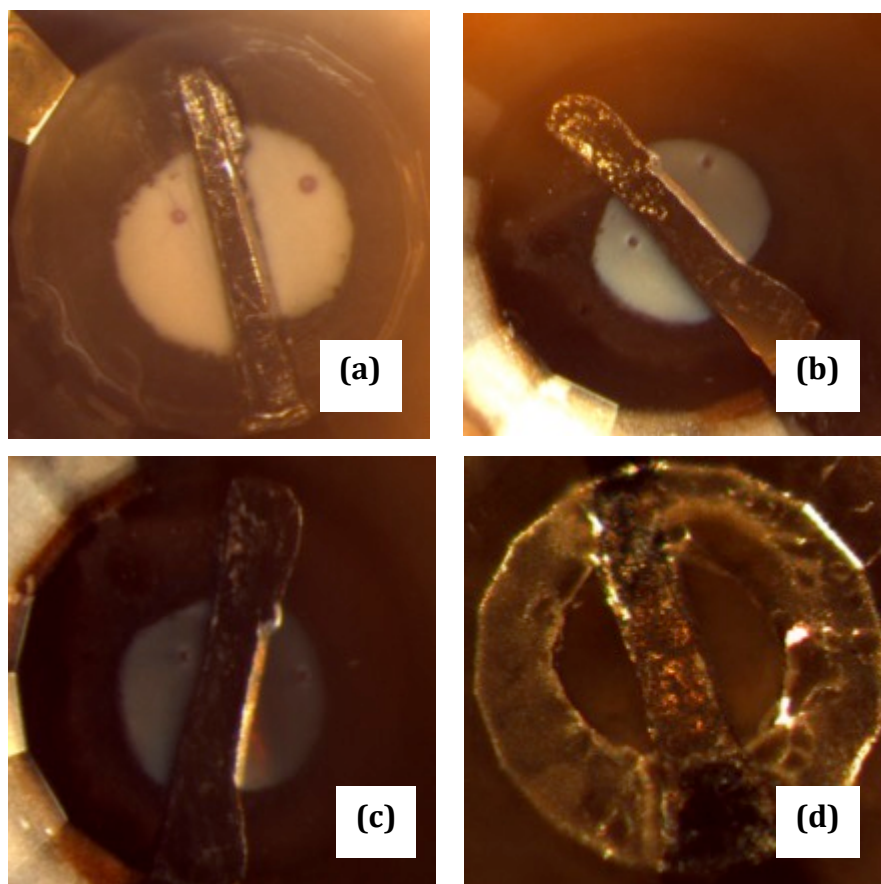


Figure 5.5: 8YSZ pictures taken after 25-250^oC heating at pressures of (a) 0Gpa, (b) 6.1GPa, (c) 17.5GPa, (d) 0GPa decompression taken outside of DA

The conductivity values were then combined into an Arrhenius plot to illustrate how the pressure effected the ionic conductivity, shown in Figure 5.6.

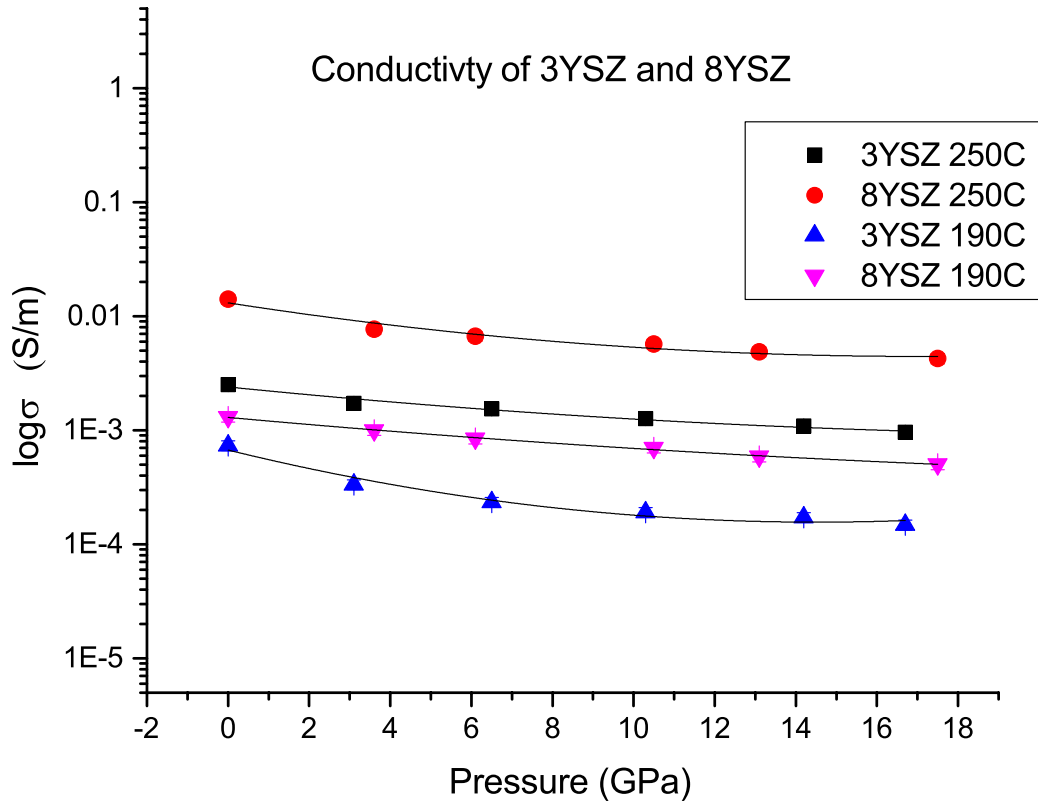


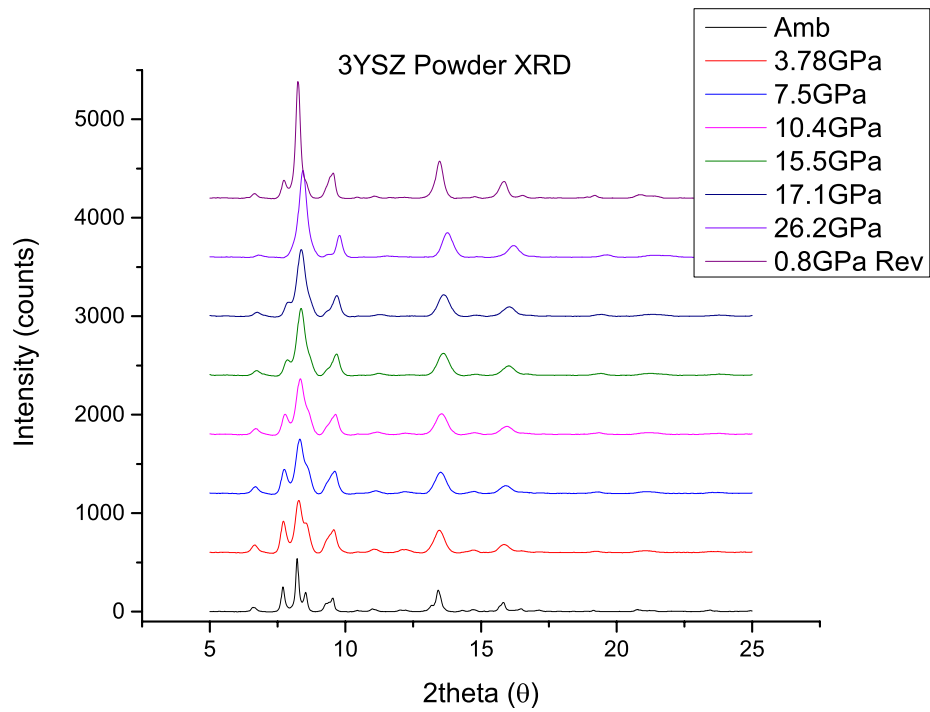
Figure 5.6: Experimental conductivities shown in the $\log \sigma$ form with respect to pressure.

As can be seen from the data, the resistance of both the 3YSZ and 8YSZ increased with pressure. The conductivities increased with temperature, corroborating past literature [12,13,14] and they decreased with pressure similar to [4]. Error associated with this data can come in many forms, although care was taken to reduce any uncertainty. The largest error may originate from the measured dimensions and thickness of the sample and electrodes. Sample temperature, thermalization of the sample, pressure measurements, pressure gradients in sample, non-

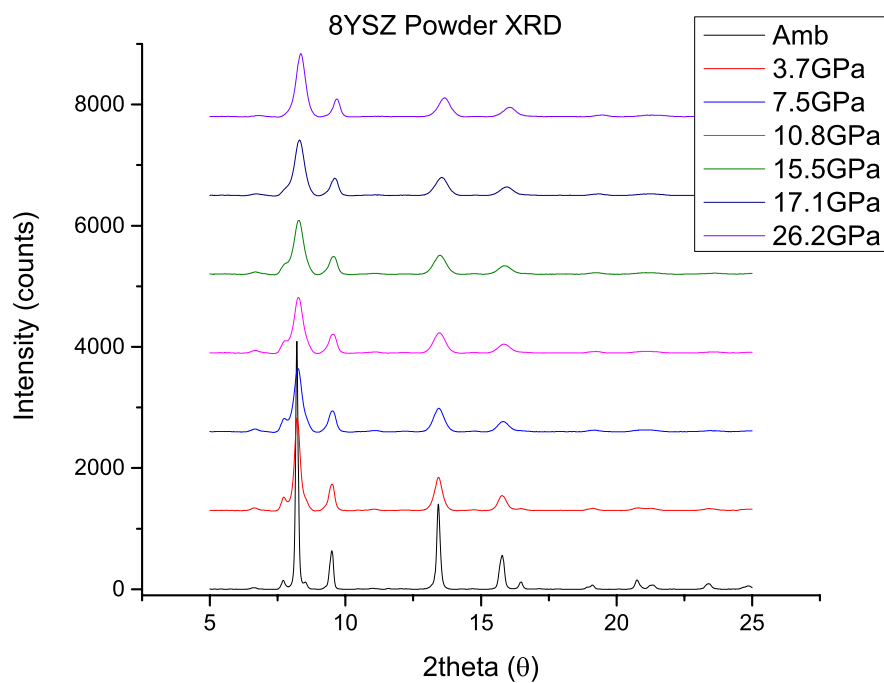
hydroticity, and hysteresis, all could add to the error of the calculated conductivity. Although no odd electrical behavior appeared in this experiment, higher pressures might cause damage to the platinum leads and therefore a sputter coating of gold or molybdenum might be a better choice for the electrical measurements. As seen in M'Peko *et al*, the ionic conductivity of 3YSZ has a stress orientation dependence. To produce a better high pressure experiment, YSZ would need to be measured under hydrostatic conditions which would help alleviate the effects caused by the non-hydrostatic uniaxial stress used in this thesis project.

NON-HYDROSTATIC HIGH-PRESSURE POWDER X-RAY DIFFRACTION STRUCTURE STUDY

The powder XRD patterns collected at the BM-D beam line at HP-CAT Sector 16 at the Advanced Photon Source were masked, integrated, and background subtracted with Dioptas software. The stacked plots of the XRD integrated patterns for the 3YSZ and 8YSZ samples is shown below in figure 5.7a and b. Due to the non-hydrostaticity of the sample, as pressure increased, the peaks broadened and intensity was affected. There appear to be no phase transitions occurring between pressures of 0-26GPa. This is the first report of 3YSZ and 8YSZ powder studied with powder XRD and pressures between 0-26GPa, so there are no publications to confirm or refute the data.



(a)



(b)

Figure 5.7: Powder XRD patterns for (a) 3YSZ and (b) 8YSZ

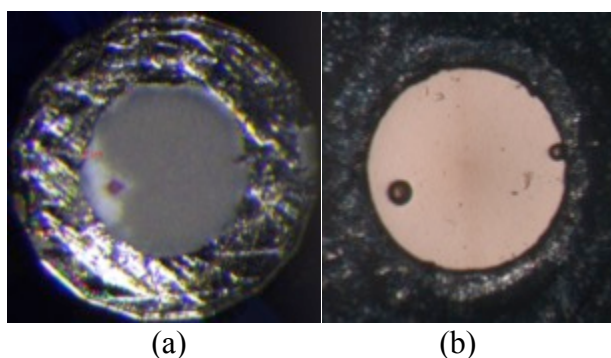


Figure 5.8: Picture of 8YSZ loaded in DAC at (a) 0 GPa and (b) 26 GPa

The XRD data was then imported into MDI Jade® software and auto indexed. The tetragonal space group $P4_2/nmc$ was the best fit for the 3YSZ and 8YSZ patterns. In past publications, a $P4_2/nmc$ space group was found to be the space group best describing 3YSZ and 8YSZ powder at ambient pressures [26] and the results from this experiment confirm those claims. As pressure was applied, the tetragonal $P4_2/nmc$ space group continued to fit the data and the volume of the cell decreased. In Table 5.2, the pressure and volume information are shown, as well as the volume error.

TABLE 5.2 Pressure and Calculated Cell Volumes

3YSZ			8YSZ		
Pressure (GPa)	Volume (\AA^3)	Error (\AA^3)	Pressure (GPa)	Volume (\AA^3)	Error (\AA^3)
0	67.39	.10	0	67.7	.11
3.6	66.45	.11	3.1	66.65	.16
6.5	65.75	.13	6.1	65.69	.12
10.3	64.95	.12	10.5	64.51	.11
14.2	64.21	.11	13.1	63.66	.13
16.7	63.82	.14	17.2	62.98	.12

TABLE 5.2: The measured pressure is displayed with the calculated cell volume and the error for the volume is also given.

The Birch-Murnaghan Equation of State (EOS) was fit to the pressure and volume data and the *non-hydrostatic* EOS was determined and the bulk modulus calculated for the 3YSZ was 206GPa and 197GPa for the 8YSZ, Figure 5.9 displays the pressure volume plot along with the EOS fit line

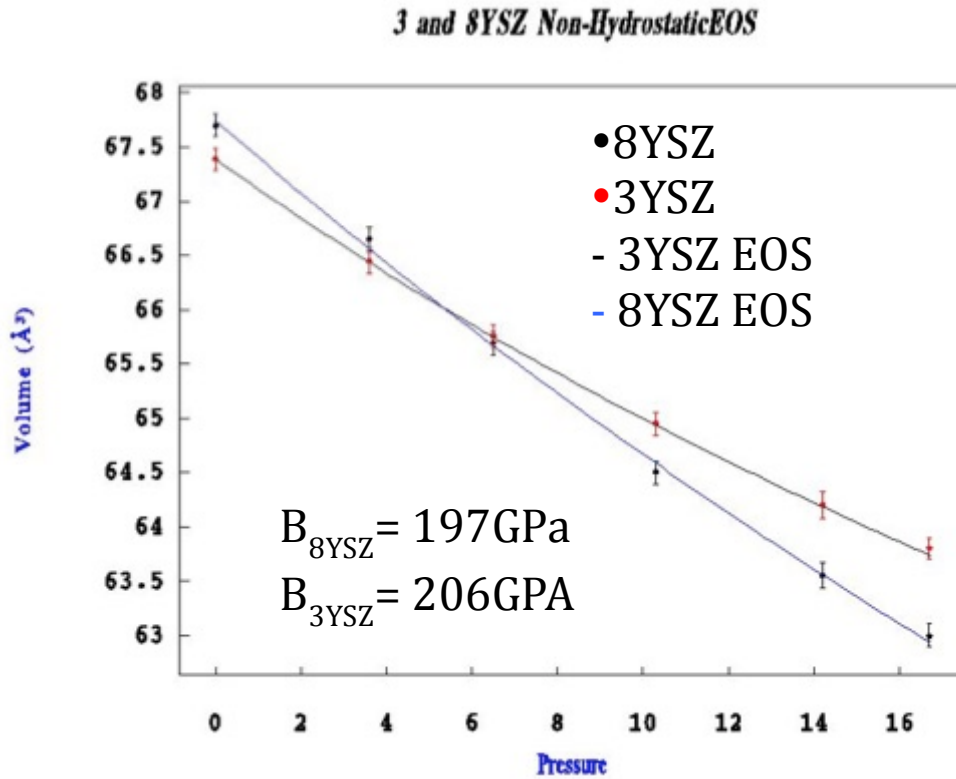


Figure 5.9: Pressure volume plot along with the EOS fit line for 3YSZ (red/black), 8YSZ (black/blue).

Considering that there is no evidence of a phase transition, the continual increase of resistance can be attributed to the increase of pressure and decrease in cell volume. In the study of M'Peko *et al*, it was concluded that the electrical conduction processes are stress dependent and probably occur from lattice distortion. The work here, achieving much higher stress states than earlier studies seem to corroborate these speculations. As the cell volume decreases, the oxygen vacancy sites can become closer together. One would expect that a closer proximity of vacancy

sites and mobile ions could encourage oxygen ion conduction, but the data clearly shows that this is not the case.

To better understand the relationship between high-pressure environments and oxygen ion conduction in YSZ, a hydrostatic high-pressure experiment reaching higher temperatures will need to be conducted. The challenges with this type of experiment will be creating a setup with a pressure-transmitting medium that will not skew the EIS measurements and be able to handle temperatures higher than 1400°C, which is the common operating temperature of a SOFC. Additionally, this technique could be applied to single crystal YSZ to investigate if there are any preferred orientations of ionic conduction. Again this type of experiment would need a pressure-transmitting medium. Furthermore, many ambient studies of YSZ ionic conductivity have investigated grain size and uniformity, so the effect of different grain size and grain boundary distribution could give insight into how ions move through YSZ under stress.

Chapter 6

CONCLUSIONS

This work presents the first impedance spectroscopic study of 3YSZ and 8YSZ at pressures of 0-17GPa and at temperatures of 25-250°C. Pressure was obtained via a diamond anvil cell and a self-made heating device enabled heating of our sample. The data collected showed that the resistance of both samples increased with pressure. The highest conductivities of both samples occurred at ambient pressure and at 250°C temperature. The conductivities of both samples at their highest pressures were a factor a magnitude less than the ambient measurements. A non-hydrostatic high-pressure powder XRD study of 3YSZ and 8YSZ occurred at HP-CAT APS ANL. A tetragonal structure with the space group $P4_2/nmc$ was confirmed for both samples and their cell parameters were reported. The volume change of the cell was also reported and the Birch-Murnaghan EOS was fitted to the data and a *non-hydrostatic* EOS was also reported. No phase changes occurred in the samples under the pressures of 0-26GPa. The data collected from this experiment shows that as stress is applied and the cell volume decreases, the conductivity also decreases. Further investigations are needed to resolve the mechanism for the decrease in conductivity under the conditions used in this experiment.

REFERENCES

1. Yanagida, H., Koumoto, K., and Miyayama, M., *John Wiley & Sons* **1** (1996)
2. López-Gándara, C., Ramos, F. M., and Cirera, A., *Journal of Sensors* **2009** (2009)
3. D. Clarke, S. R. Phillpot, *Materials Today* **8**, Issue 6, (2005) 22-29.
4. M'Peko, J., Spavieri, D. L., and de Souza, M. F. *Applied Physics Letters* **81**, (2002) 2827-2829.
5. Grafov, B.M. and Ukshe, E.A., *Nauka*, (1973) 128.
6. Solov'eva, L.M., *Sverdlovsk Ural Otd. Akad. Nauk* (1981) 68–82.
7. Babushkina, G.V. and Kobelev, L.Ya., *Vysokomol. Soedin. Ser. B*, **30** (1988) 643–644.
8. Vereshchagin, A.F., Yakovlev, E.N., Stepanov, G.N., et al., *Pis'ma Zh. Eksp. Teor. Fiz.*, **16** (1972) 240–242.
9. Goettel Kenneth, A. Mao, H. and Bell, P. M., *Review of Scientific Instruments*, **56** (1985) 1420-1427.
10. Pistorius, C., *Progress in Solid State Chemistry* **11** (1976) 1-151.
11. Caron, L. G., *Physical Review B* **9**, 12 (1974) 5025.
12. Meĭerovich, B. É., *Physics-Uspekhi* **29**, 6 (1986) 506-529.
13. Valyanskaya, T. V., and Stepanov., G. N., *Solid State Communications* **86**, 11 (1993) 723-725.
14. He, C., Liu, B., Li, M., and Gao, C., *Review of Scientific Instruments*, **82**, 015104 (2011)
15. Han, Y. H., Wang, H. B., Troyan, I. A., and Gao, C. X., Eremets, M. I., *The Journal of Chemical Physics*, **140**, 044708 (2014).
16. Sun, J., Clark, B. K., Torquato, S., and Car, R., *Nature Communications* **6** (2015) 8156.
17. Price, G. D., *Elsevier*, **2** (2009).

18. Voevodin, A. A., Zabinski, J. S., Muratore, C., *Tsinghua Science & Technology* **10**, 6, (2005) 665-679.
19. Badwal, S., *Solid State Ionics*, **52**, 1-3 (1992) 23–32.
20. Xin, X. *University College London*, (2010)
21. http://www.doitpoms.ac.uk/tlplib/fuel-cells/sofc_electrolyte.ph
22. Yashima, M., Mitsushashi, T., Takashina, H., Kakihana, M., Ikegami, T. and Yoshimura, M., *Journal of the American Ceramic Society*, **78** (1995) 2225–2228.
23. Yashima, M., Hirose, T., Katano, S., Suzuki, Y., Kakihana, M., and Yoshimura, M., *Phys. Rev. B*, **51** (1995) 8018
24. Du, Y., Jin, Z., and Huang, P., *J. Am. Ceram. Soc.* **74** (1991) 1569
25. Lamas, D. G. and Walsoe de Ruca, N., *Jounral of Material Science*, **35**, 22 (2000) 5563-5567.
26. Yashima, M., Kakihana, M., and Yoshimura, M., *Solid State Ionics*, **86–88**, 2 (1996) 1131-1149.
27. Corradi, A. B., Bondioli, F., and Ferrari, A. M., *Chem. Mater.* **13** (2001) 4450.
28. Yashima, M., Morimoto, K., Ishizawa, N., and Yoshimura, M. J., *J. Am. Ceram. Soc.* **76** (1993) 1745.
29. Ioffe, I. A., Rutman, D.S., and Karpachov, S.V., *Electro. chim. Acta*, **23**, 141 (1978).
30. Badwal, S. P., *Solid State Ionics* **52**, 23 (1992).
31. Khan, M., Islam, M., and Bates, D., *J. Mater. Chem.* **8**, 2299 (1998).
32. Kilo, M., Jackson, R., and Borshardt, G., *Philos. Mag.*, **83**, 3309 (2003).
33. Zavodinsky, V., *Phys. Solid State*, **46**, 453 (2004).

34. Krishnamurthy, R., Yoon, Y., Srolovitz, D., and Car, R., *J. Am. Ceram. Soc.* **87**, 1821 (2004).
35. Martin, M., *Phys. Chem.* **219**, 105 (2005).
36. Alzyab, B., Perry, C. H., and Ingel, R. P., *Journal of the American Ceramic Society*, **70** (1987) 760–765.
37. Ichiyanagi, K. and Nakamura, K., *Metals*, **6**, 1 (2015).
38. Macdonald, D. D., *Electrochimica Acta*, **51**, 8-9, (2006) 1376–1388.
39. Macdonald, J. R., *John Wiley & Sons*, **2** (1987)
40. Mccann, J. F. and Badwal, S. P.S., *J. Electrochem. Soc.* **129**, 3 (1982) 55
41. Hooper, A., *AERE-R*, **9757** (1980)
42. Retter, U. and Lohse, H., *Springer* (2002) 149–166.
43. Chen, R., Chen, L.-F., and Chia, C.-T., *Journal of Physics: Condensed Matter*, **19**, 8, (2007) 086225.
44. Pimenov, A., Ullrich, J., Lunkenheimer, P., and Loidl, A., *Solid State Ionics*, **109**, 1-2 (1998) 111 – 118.
45. Bauerle, J., *Journal of Physics and Chemistry of Solids*, **30**, 12 (1969) 2657 – 2670.
46. Beekmans, N., and Heyne, L., *Electrochimica Acta*, **21**, 4 (1976) 303 – 310.
47. van Dijk, T. and Burggraaf, A. J., *Physica Status Solidi A* **63**, 1 (1981).229-240.
48. Abouzari, M. S., Berkemeier, F., Schmitz, G., and Wilmer, D., *Solid State Ionics*, **180**, 14-16 (2009) 922 – 927.
49. Mao, H. K., Xu, J., and Bell, P. M., *J. Geophys. Res.* **91** (1986) 4673.
50. Rekhi, S., Dubrovinsky, L.S., and Saxena, S.K. *High Temp. - High Pres.* **31** (1999) 299.

51. <https://web.phys.ksu.edu/vqm/laserweb/Ch-6/F6s2t1p2.htm>
52. Bragg, W. L., *Proceedings of the Royal Society of London. Series A*, **89**, 6102 (1913) 48–277.
53. Debye, P. and Scherrer, P., *Mathematisch-Physikalische Klasse*, **1916**, (1916) 1–15.
54. Kittel, C., “Introduction to Solid State Physics”, *Wiley* **1** (1966).
55. Ashcroft, N.W. and Merimin, D., “Introduction to Solid State Physics”, *Holt, Rhinehart, and Wilson* **1** (1976).
56. Boultif, A. and Louër, D., *Journal of Applied Crystallography*, **24** (1999) 987–993.
57. Baker, J., *UNLV* (2012).

CURRICULUM VITAE

GRADUATE COLLEGE

UNIVERSITY OF NEVADA, LAS VEGAS

QUINLAN SMITH

EMAIL: QUINN.B.SMITH@GMAIL.COM

Education

M.S. in Physics. (2012 – May 14, 2016)

University of Nevada, Las Vegas

B.S. in Physics, (2008-2012)

California Lutheran University

Awards and Activities

NNSA NSSC MSI Summer Graduate Fellow

Summer 2015

Work Experience-

NNSA NSSC LANL-SNL Summer School (August 3-12, 2015)

- Learned and participated in destructive and non-destructive assay techniques for special nuclear material verification
- Learned about nuclear nonproliferation policy and implementation

NNSA NSSC-MSI Summer Fellow LLNL (Summer 2015)

- Advisor: Dr. Natalia Zaitseva, Dr. Andrew Glenn
- Developed coded aperture imaging for neutron detection
- Synthesized/characterized plastic scintillating materials for neutron and gamma radiation detection

Research Assistant – UNLV – Department of Physics (2012-present)

- Advisor: Dr. Michael Pravica
- High Pressure Science and Engineering Center Graduate Researcher
- Studying ionic conductivity of $\text{La}_{(2/3-x)}\text{Li}_x\text{TiO}_3$ under extreme conditions
- Studied the oxygen pathways of irradiation damaged KClO_4
- Researching materials under extreme conditions

Teacher Assistant – UNLV – Department of Physics (2012-present)

- Taught Intro Physics (algebra/calculus base) Laboratory sections
- Lecture and educate college students about physics through Laboratory experiments

Research Experience for Undergraduates – UNLV – High Pressure science and Engineering Center (Summer 2011)

- Advisor: Dr. Pamela Burnley
- Researched the correlation between crystallographic orientation and deformation planes

Research Experience for Undergraduates – Washington State University – Institute for Shock Physics (Summer 2010)

- Advisor: Dr. Choong-shik Yu
- Researched the magnetic effects on materials under extreme conditions

Research Experience-

- **DOE Radiological Worker 1 Certified** (June 2015)
- **National Lab Experience:**
 - Countless hours of research at National Labs- (APS - ANL, Canadian Light Source, Positive Ion Accelerator -Naval Surface Warfare Research Center-(NSWCCD), Lawrence Livermore National Laboratory, Los Alamos National Lab, Sandia National Lab
- **Experienced in High Pressure Physics**
 - Diamond Anvil Cells (PEC, Symmetric, Mao-Bell, Panoramic)
 - Electronic Discharge Machining/Laser Drilling (Stainless Steel, Rhenium, Beryllium)
 - X-ray Diffraction
 - Raman Spectroscopy
 - Scanning Electron Microscopy
 - Laser Heating
 - IR Spectroscopy (Mid-IR, Far-IR)
 - X-Ray Raman Spectroscopy

- X-Ray Absorption Near Edge Spectroscopy
 - Electron Backscatter Diffraction
 - 4-probe resistance measurements
 - Impedance Spectroscopy
- **Programs**
 - (Origin Pro, Fit-2D, Opus, Fityk, Sigma-Plot, Jade, Dioptas, Powder Cell, VESTA, Fit-2D, EOSFit7)

Publication

- “High Pressure x-ray photochemical studies of carbon tetrachloride: Cl₂ production and segregation,” M. Pravica, D. Sneed, Q. Smith, L. Bai, *Chemical Physics Letters* **530**, pp. 74-76 (2013).
- “X-ray induced mobility of molecular oxygen at extreme conditions” M. Pravica, D. Popov, S. Sinogeikin, D. Sneed, G. Guardala, Q. Smith, *Applied Physics Letters*, **103**, 224103 (2013).
- “Carbon tetrachloride under extreme conditions” M. Pravica, D. Sneed, Q. Smith, *Journal of Chemical Physics*, **140**, 194503 (2014).
- “High Pressure Spectral Studies of Gallium Nitride”, M. Pravica, Y. Wang, D. Sneed, Q. Smith *Journal of Applied Physics*, submitted for publication April 7th, 2015

Poster Presentations-

- HPCAT Workshop on Advances in Matter under Extreme Conditions, October 2013- Hydrazine at High Pressure
- University & Industry Technical Interchange Review Meeting 2013- Studies of X-Ray Induced Decomposition of Alkali Halates
- 2013 Stewardship Science Academic Programs (SSAP) Annual Review Symposium- Studies in useful hard x-ray induced chemistry: Urea and CCl₄ Under Extreme Conditions
- DOE NNSA/NV-UNLV Stewardship Science Academic Alliances Program, High Pressure Science and Engineering Center, 2013 Review- X-Ray induced Mobility of Molecular Oxygen
- NNSA HiPSEC Annual Review, February 2014- Irradiation Induced Conductivity of KClO₃
- NNSA HiPSEC Annual Review, February 2015- Irradiation Induced Conductivity of KClO₄
- NNSA SSAP Annual Conference March 2015- Irradiation Induced Conductivity of Perchlorates
- NNSA NSSC LANL-SNL Summer School August 2015- Studies of Ionic Conductivity Under Extreme Conditions